Processes Preventing the Development of a Significant Tornado in a Colorado Supercell on 26 May 2010

SHAWN S. MURDZEK, PAUL M. MARKOWSKI, AND YVETTE P. RICHARDSON

The Pennsylvania State University, University Park, Pennsylvania

ROBIN L. TANAMACHI

Purdue University, West Lafayette, Indiana

(Manuscript received 30 August 2019, in final form 12 February 2020)

ABSTRACT

A supercell produced a nearly tornadic vortex during an intercept by the Second Verification of the Origins of Rotation in Tornadoes Experiment on 26 May 2010. Using observations from two mobile radars performing dual-Doppler scans, a five-probe mobile mesonet, and a proximity sounding, factors that prevented this vortex from strengthening into a significant tornado are examined. Mobile mesonet observations indicate that portions of the supercell outflow possessed excessive negative buoyancy, likely owing in part to low boundary layer relative humidity, as indicated by a high environmental lifted condensation level. Comparisons to a tornadic supercell suggest that the Prospect Valley storm had enough far-field circulation to produce a significant tornado, but was unable to converge this circulation to a sufficiently small radius. Trajectories suggest that the weak convergence might be due to the low-level mesocyclone ingesting parcels with considerable crosswise vorticity from the near-storm environment, which has been found to contribute to less steady and weaker low-level updrafts in supercell simulations. Yet another factor that likely contributed to the weak low-level circulation was the inability of parcels rich in streamwise vorticity from the forward-flank precipitation region to reach the low-level mesocyclone, likely owing to an unfavorable pressure gradient force field. In light of these results, we suggest that future research should continue focusing on the role of internal, storm-scale processes in tornadogenesis, especially in marginal environments.

1. Introduction

Tornadoes pose a serious threat to human lives. From 2003 to 2015, tornadoes were responsible for over one thousand deaths in the United States (SPC 2018). In an effort to reduce tornado-related deaths, it is important to accurately forecast tornadic storms and convey these forecasts effectively to the public. Unfortunately, it is difficult to forecast exactly when and where a tornado will occur. For example, from 2003 to 2015, only about two-thirds of tornadoes occurred in tornado-warned areas and about three-fourths of tornado warnings were never associated with a tornado (Anderson-Frey et al. 2016). One way to improve the probability of detection for tornadoes and reduce the number of false alarms is to better understand the conditions and processes that result in tornadogenesis or tornadogenesis failure.

a. Tornadogenesis within supercells

Owing to the disproportionate number of significant tornadoes[1] produced by supercells compared to other storm modes, tornadogenesis research has focused primarily on supercells (e.g., Davies-Jones 2015; Markowski and Richardson 2009). A supercell is a thunderstorm that possesses a rotating updraft; the region of rotation is termed a mesocyclone (Davies-Jones 2015). Supercells possess several unique characteristics compared to ordinary convection, including the ability to persist for several hours in a near-steady state and propagate in a deviant direction from the mean wind (Browning 1964; Davies-Jones 2015). Owing to the attention supercells received from the severe-storms community, much is known about their structure (e.g., Browning 1964; Brandes 1978;

Corresponding author: Shawn S. Murdzek, smurdzek@psu.edu

[1] Significant tornadoes are those rated ≥F2/EF2 on either the Fujita (F) or enhanced Fujita (EF) scales. The National Weather Service adopted the EF scale on 1 February 2007.

DOI: 10.1175/MWR-D-19-0288.1

Lemon and Doswell 1979; Beck and Weiss 2013), their dynamics (e.g., Rotunno and Klemp 1982, 1985; Klemp and Rotunno 1983), and environments favorable for their formation (e.g., Weisman and Klemp 1982, 1984).

Tornadogenesis within a supercell, in the absence of preexisting vertical vorticity near the surface, can be conceptualized in three distinct steps (e.g., Davies-Jones 2015). First, horizontal vorticity associated with environmental vertical wind shear is tilted by an updraft to produce vertical vorticity aloft. When the tilted horizontal vorticity is streamwise, the updraft and vertical vorticity regions coincide (Rotunno 1981; Davies-Jones 1984), forming the midlevel mesocyclone. Second, vertical vorticity must develop near the surface. Previous studies have found that downdrafts play an important role in this step (e.g., Davies-Jones and Brooks 1993) and that the vorticity bound for the surface is often augmented by baroclinic generation (Klemp and Rotunno 1983; Rotunno and Klemp 1985; Dahl 2015). Third, vertical vorticity near the surface is amplified to tornado strength by stretching. Modeling studies have found that intense stretching requires a low-level mesocyclone[2] of adequate strength so that a strong, upward-directed dynamic vertical perturbation pressure gradient force (VPPGF), related to $\partial(\zeta^2)/\partial z$, where ζ is vertical vorticity, develops in the lowest few hundred meters AGL (Markowski and Richardson 2014). This further requires that the low-level mesocyclone is positioned above significant near-surface circulation (Guarriello et al. 2018), and that the vertical vorticity-rich air parcels near the surface are not too negatively buoyant so they can be accelerated upward within the low-level mesocyclone (Markowski and Richardson 2014).

Beyond the environmental conditions needed to produce supercells (e.g., convective available potential energy [CAPE] and strong deep-layer [0–6 km] shear), other conditions have been recognized as being conducive for tornadogenesis. In particular, low lifted condensation levels (LCL) and strong 0–1 km storm-relative helicity (SRH) values are favorable for tornadogenesis (Thompson et al. 2003). Low LCLs correspond to high relative humidity values in the boundary layer, which tend to result in decreased evaporational cooling in supercell outflow. This keeps the outflow from possessing excessive negative buoyancy and increases the chance that vorticity-rich (either horizontal or vertical vorticity) parcels can be "sucked up" by the overlying updraft, thereby leading to explosive vertical vorticity amplification next to the surface via tilting and stretching (Markowski and Richardson 2009, 2014). The flux of streamwise, horizontal vorticity over the lowest kilometer into a supercell is related to the 0–1 km SRH. When 0–1 km SRH is large and the flux of horizontal, crosswise vorticity is small, there is a large correlation between positive vertical velocity and positive vertical vorticity (Davies-Jones 1984), leading to a more coherent low-level mesocyclone closer to the ground. Thus, large 0–1 km SRH values tend to favor stronger low-level mesocyclones that have a stronger suction force (i.e., upward-directed VPPGF) owing to a better collocation between the vertical velocity and vertical vorticity maxima within the low-level mesocyclone and the close proximity of the base of the low-level mesocyclone to the ground (Markowski and Richardson 2014). This stronger low-level mesocyclone can more effectively stretch near-surface vertical vorticity.

One tornado forecasting challenge is that supercells can exist in environments favorable for tornadogenesis without producing tornadoes, and occasionally supercells can become tornadic in unfavorable environments. This is best seen in Fig. 12 of Craven and Brooks (2004), which shows considerable overlap between tornadic and nontornadic supercell environments within the 0–1 km shear and LCL parameter space. The fact that no combination of environmental parameters has been found to perfectly discriminate between the environments of tornadic and nontornadic supercells suggests that internal processes within a supercell (which are not easily predicted by the environmental parameters used by forecasters) as well as interactions with other mesoscale features (such as fronts and other convection) also play a vital role in tornadogenesis or tornadogenesis failure.

b. *Observations of tornadogenesis failure*

In an effort to better understand the processes that can lead to tornadogenesis failure in environments favorable for tornadic supercells, several observational studies have examined the characteristics of nontornadic supercells. The earliest studies to methodically examine the differences between tornadic and nontornadic supercells used data collected during the first Verification of the Origins of Rotation in Tornadoes Experiment (VORTEX1; Rasmussen et al. 1994). Early analyses of VORTEX1 cases using pseudo-dual-Doppler wind syntheses from airborne radars found that tornadic and

[2] In this study, "low-level" refers to altitudes below 1000 m; however, "near-surface" is used to distinguish the lowest 50 m from the rest of the "low-level" atmosphere. This distinction is important because numerical simulations have shown that near-surface vertical vorticity requires the development of outflow and downdrafts, unlike vertical vorticity at higher altitudes. Horizontal vorticity within the outflow, which ultimately contributes to the near-surface vertical vorticity, is greatly enhanced by baroclinic generation and horizontal stretching (Rotunno and Klemp 1985; Markowski and Richardson 2014; Rotunno et al. 2017) and can sometimes be tilted into the vertical as parcels descend in downdrafts (Davies-Jones and Brooks 1993).

TABLE 1. Modes of tornadogenesis failure identified in observed, nontornadic low-level mesocyclones and modeling studies of nontornadic supercells.

Mode of tornadogenesis failure	References
Excessive negative buoyancy in the outflow (possibly owing to high LCLs)	Markowski et al. (2002), Shabbott and Markowski (2006), Grzych et al. (2007), and Markowski and Richardson (2014)
Disorganized low-level updraft owing to significant crosswise vorticity and insufficient streamwise vorticity in the low-level, near-storm environmental inflow	Beck et al. (2006), Coffer and Parker (2017), Coffer et al. (2017), and Coffer and Parker (2018)
Short time period of favorable conditions	Skinner et al. (2014)
Descending reflectivity core	Markowski et al. (2018)
Storm merger	Klees et al. (2016)
Near-surface vertical vorticity not positioned beneath the updraft	Guarriello et al. (2018)
Rapid low-level mesocyclone cycling owing to strong outflow undercutting the updraft	Beck et al. (2006) and Bowlan (2013)

nontornadic supercells are nearly identical on the mesocyclone-scale, with both types of supercells exhibiting low-level mesocyclones, occlusion downdrafts, and comparable low-level vertical vorticity values (Trapp 1999; Wakimoto and Cai 2000).

Seeing few kinematic differences between tornadic and nontornadic supercells at the mesocyclone scale, other studies focused on thermodynamic differences. Using surface observations from a mobile mesonet operated during VORTEX1, Markowski et al. (2002) found that tornadic storms tend to have less negatively buoyant rear-flank outflow (RFO) compared to nontornadic storms, which may be partially attributable to the higher LCLs in these nontornadic environments. The conclusion reached by Markowski et al. (2002) was supported by Grzych et al. (2007) and also extended to the forward-flank outflow by Shabbott and Markowski (2006). Even among these studies, however, there were some instances of supercells with outflow that did not possess excessive negative buoyancy but still did not produce a tornado. This led to the conclusion that having outflow that is not excessively negatively buoyant is a necessary, but insufficient, condition for tornadogenesis.

Other studies examined whether tornadogenesis failure could be attributed to a lack of baroclinic generation of vorticity. Markowski et al. (2008, 2011) used pseudo-dual-Doppler and ground-based dual-Doppler wind syntheses, respectively, to compute vortex lines for tornadic and nontornadic supercells. These two studies found arching vortex lines with horizontal projections that were oriented in a way that was inferred to be indicative of baroclinic generation of vorticity. These results, combined with the fact that Shabbott and Markowski (2006) found weaker near-surface buoyancy gradients in the forward flank of tornadic supercells, suggests that while baroclinic generation of vorticity may be important for tornadogenesis, lack of sufficient baroclinic generation does not appear to be a common mode of tornadogenesis failure.

A number of case studies of nontornadic supercells from the early 2000s and during the Second Verification of the Origins of Rotation in Tornadoes Experiment (VORTEX2; Wurman et al. 2012) as well as a few modeling studies have identified several other modes of tornadogenesis failure. These failure modes are summarized in Table 1. Perhaps most notable is Coffer and Parker (2017) and Coffer et al. (2017), who found using an idealized model that small differences in the low-level wind profile in the near-inflow of a supercell have a large impact on whether or not tornadogenesis will occur. Specifically, excessive amounts of near-inflow crosswise vorticity and little near-inflow streamwise vorticity resulted in supercells with weaker and more disorganized low-level mesocyclones, which resulted in tornadogenesis failure.

Even though multiple studies of tornadogenesis failure have been presented here, there are many more studies focused on tornadogenesis. This is a weakness of the tornado literature because there are several modes of tornadogenesis failure and very few have been scrutinized closely. By investigating the ways tornadogenesis failure occurs, we can better forecast which storms will not be tornadic, reducing the false alarm ratio. This study seeks to advance our understanding of tornadogenesis failure by exploring why the 26 May 2010 supercell near Prospect Valley, Colorado (hereafter referred to as the Prospect Valley storm), intercepted by VORTEX2 failed to produce a significant tornado during a 20-min observation period.

c. *Overview of the Prospect Valley storm*

The Prospect Valley storm was initiated around 1845 UTC in a region of upslope flow in the Denver metropolitan area. Southeasterly low-level flow in the southern Great Plains over the previous 24 hours advected moisture from the Gulf of Mexico into Colorado, contributing to values of CAPE exceeding $1000\,\mathrm{J\,kg^{-1}}$ (Table 2 and Fig. 1). The vertical wind profile in the

TABLE 2. Parameters from the smoothed 2223 UTC NSSL1 MGAUS (see section 2b). For LCL height, CAPE, and CIN, mixed-layer values are presented with surface-based values given in parentheses. Mixed-layer parameters were computed using a parcel that possessed the average characteristics of the lowest 50 hPa of the MGAUS. The 0–6 km bulk wind difference is computed using the mean wind over the lowest 500 m AGL as the surface wind. SRH is computed using the observed storm motion of (4.45, 3.51) $m\,s^{-1}$.

Parameter	Value
0–500 m SRH	40.3 $m^2\,s^{-2}$
0–1 km SRH	70.0 $m^2\,s^{-2}$
0–3 km SRH	210.9 $m^2\,s^{-2}$
0–1 km bulk wind difference	6.5 $m\,s^{-1}$
0–6 km bulk wind difference	21.0 $m\,s^{-1}$
LCL Height	1499 m (1352 m)
CAPE	1092 $J\,kg^{-1}$ (1410 $J\,kg^{-1}$)
CIN	21 $J\,kg^{-1}$ (22 $J\,kg^{-1}$)

Denver metropolitan area was also conducive for supercells with a 0–6 km bulk wind difference of 21.0 $m\,s^{-1}$ and a 0–3 km SRH value of 210.9 $m^2\,s^{-2}$. Owing to these favorable conditions, the Prospect Valley storm developed supercellular characteristics, including a hook echo, as seen in the Denver Weather Surveillance Radar-1988 Doppler (WSR-88D) reflectivity scans (Fig. 2). The Prospect Valley storm proceeded to move slowly to the east-northeast over the next several hours. During this time, there were several associated severe storm reports made to the Storm Prediction Center (SPC), including five tornado reports between 1930 and 2110 UTC. No additional tornadoes were reported in association with the Prospect Valley storm after 2110 UTC (SPC 2010). Because these tornadoes occurred before the VORTEX2 deployment, a further analysis of the tornadic phase of the Prospect Valley storm is not included in this article.

The VORTEX2 armada declared the Prospect Valley storm the target at 2110 UTC and started sampling the storm at 2150 UTC. Between 2218 and 2247 UTC, seven sub-tornado-strength, convective-storm vortices (SCVs) were observed by the UMass W-band radar (Tanamachi et al. 2013). One of these SCVs, SCV 5, met the criterion of a tornado commonly used in Doppler on Wheels (DOW) observational studies (inbound-outbound velocity difference of 40 $m\,s^{-1}$ across $\leq$ 2 km, e.g., Alexander and Wurman 2008), but was not classified as a tornado by the SPC because it did not produce a visible funnel cloud, visible debris cloud, or EF0 surface damage (Tanamachi et al. 2013). Owing to the fact that SCV 5 is "at the fuzzy lower boundary of what constitutes a tornado" (Tanamachi et al. 2013, p. 3662), it is unclear as to whether the intensification of SCV 5 to near-tornado strength should be referred to as "tornadogenesis" or "tornadogenesis failure." Therefore, we will refrain from using either term when discussing SCV 5 and instead

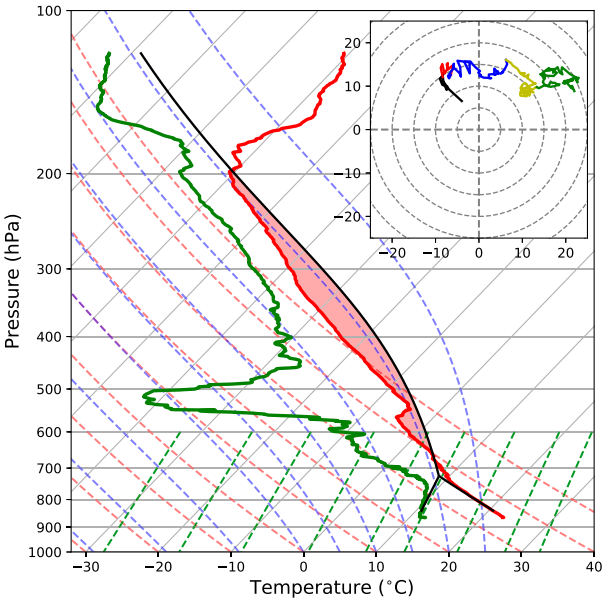

FIG. 1. 2223 UTC NSSL1 MGAUS. Temperature (red), dewpoint (green), and mixed-layer parcel (black) profiles are plotted on the skew T–log$p$ diagram along with dry adiabats (dashed red), moist adiabats (dashed blue), and constant mixing ratio lines (dashed green). The red shaded area is proportional to the CAPE for a mixed-layer parcel (which is 1092 $J\,kg^{-1}$). For the hodograph, range rings are included every 5 $m\,s^{-1}$ and the black, red, blue, yellow, and green line segments correspond to the winds between 0–0.5, 0.5–1, 1–3, 3–6, and 6–9 km, respectively.

frame the discussion in terms of processes that prevented SCV 5 from intensifying into a strong, significant tornado during the 2225–2245 UTC observation time period. Observations used for this analysis include coordinated dual-Doppler scans collected by DOW6 and DOW7, five mobile mesonet probes (Straka et al. 1996; Waugh and Fredrickson 2010) operated by the Pennsylvania State University and the National Severe Storms Laboratory (NSSL), and one Mobile GPS Advanced Upper Air Sounding System (MGAUS) operated by NSSL. Figure 2 shows the location of the DOWs and MGAUS relative to the Prospect Valley storm.

It is worth noting that the Prospect Valley storm was the topic of a 2013 M.S. thesis at the University of Oklahoma (Bowlan 2013). Using dual-Doppler wind syntheses derived from DOW data and mobile mesonet observations, Bowlan (2013) concluded that the failure for SCV 5 to further intensify was the result of a strong occlusion downdraft[3] that caused the rear-flank gust front to surge well ahead of the low-level mesocyclone,

[3] We refer to this feature as a "warm downdraft" in this study because it is not clear whether this feature formed in a manner similar to that of an occlusion downdraft.

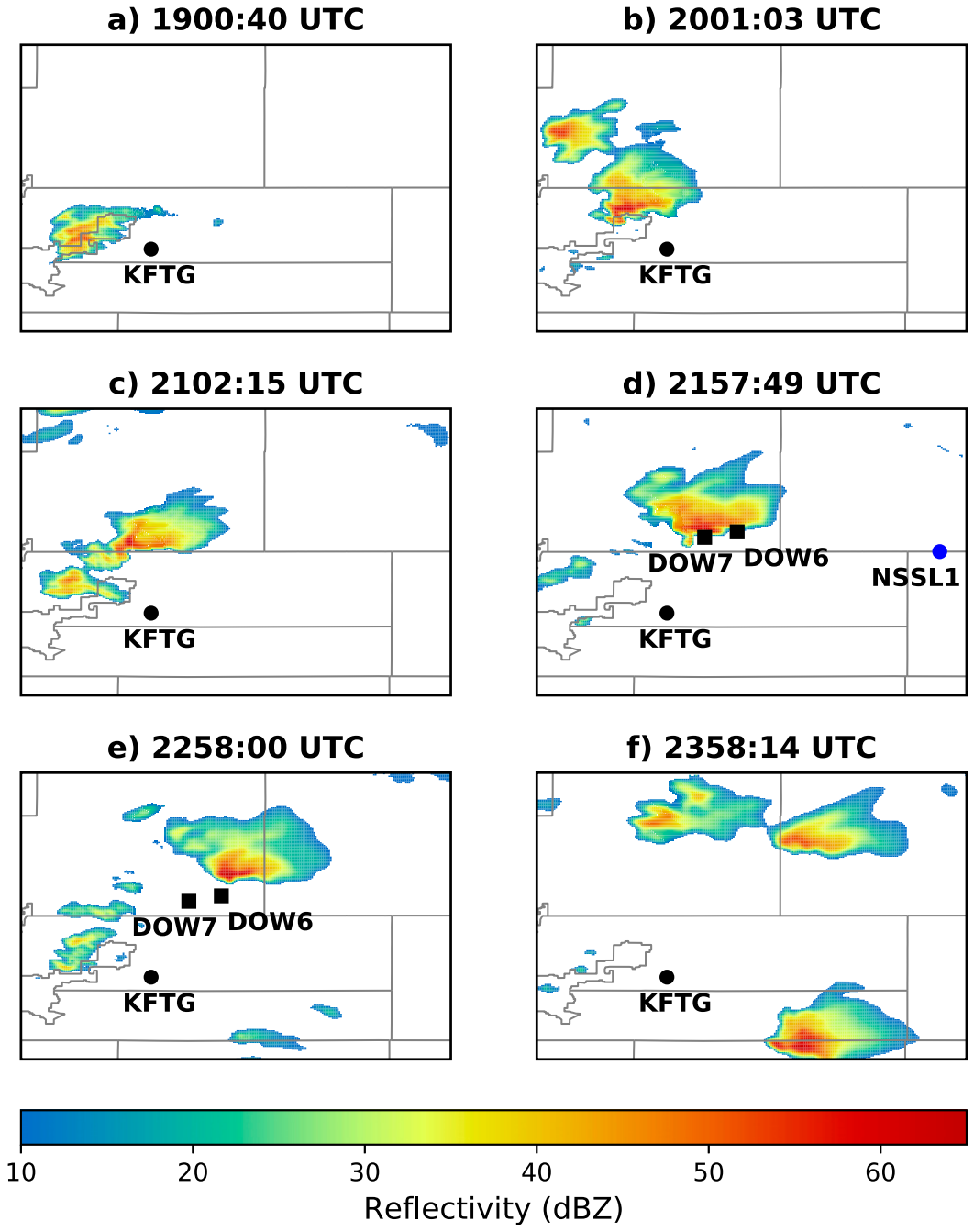

FIG. 2. Prospect Valley storm reflectivity at 1.5 km AGL from the Denver, CO, WSR-88D (KFTG) at (a) 1900:40, (b) 2001:03, (c) 2102:15, (d) 2157:49, (e) 2258:00, and (f) 2358:14 UTC 26 May 2010. The black dot is the KFTG radar site, the black squares are the DOW locations (during the 2218–2302 UTC deployment), the blue dot is the NSSL1 MGAUS launch site (launched at 2223 UTC), and the gray lines show county borders.

removing the low-level mesocyclone from the inflow air. Had the low-level mesocyclone been stronger or the occlusion downdraft been located closer to the low-level mesocyclone, Bowlan (2013) postulated, the outflow from the occlusion downdraft may have ''circulated around the mesocyclone'' (Bowlan 2013, p. 68) instead of driving the rear-flank gust front eastward, and SCV 5 may have further intensified. An independent analysis is conducted in this article that focuses on why the low-level mesocyclone was weaker, and other impacts the strong downdraft south of the low-level mesocyclone had on the evolution of SCV 5. This alternative

TABLE 3. Doppler on Wheels specifications for the Prospect Valley storm. "Update time" refers to the amount of time required to scan a single three-dimensional volume. For wavelength, maximum unambiguous velocity, and maximum unambiguous range, the two values correspond to DOW6 and DOW7, respectively.

Wavelength	3.19, 3.21 cm
Beamwidth	0.9°
Update time	2 min
Maximum unambiguous velocity	23.46, 23.09 m s^{-1}
Maximum unambiguous range	50.9, 52.0 km
Radial gate spacing	59.96 m
Elevation angles in a volume	0.5°, 1.0°, 2.0°, 3.0°, 4.0°, 5.0°, 6.0°, 8.0°, 10.0°, 12.0°, 14.0°

perspective, along with applying analysis methods not used in Bowlan (2013), such as parcel trajectories, azimuthally averaged fields, and pressure retrievals, complements the work of Bowlan (2013).

The remainder of this article is organized as follows: section 2 provides an overview of the data processing applied to the VORTEX2 observations. Section 3 presents some general observations from the Prospect Valley storm. Section 4 compares the Prospect Valley storm to the tornadic Goshen County storm. Motivated by the results from sections 3 and 4, section 5 examines two sets of trajectories to better understand why the low-level mesocyclone of the Prospect Valley storm was relatively weak. Section 6 provides a discussion related to the inability of the Prospect Valley storm to ingest parcels from the forward flank rich in streamwise vorticity, and section 7 summarizes the main results of this article.

2. Methods

a. Mobile radar data processing

DOW scans were used to retrieve the three-dimensional wind field of the Prospect Valley storm every 2 min[4] during the dual-Doppler period, which lasted from 2218 to 2302 UTC. Specifications of the DOWs are presented in Table 3. The process of creating three-dimensional wind syntheses from dual-Doppler data has been well documented by several other studies (e.g., Brandes 1977; Markowski et al. 2012a; Klees et al. 2016) and is also reviewed here. The DOW radar data were first manually edited using the SOLO 3 software package (Oye et al. 1995) to remove ground clutter and other spurious echoes as well as to dealias velocities. After editing, DOW data were objectively analyzed onto a Cartesian grid that moved with the mean storm motion using a two-pass, isotropic Barnes objective analysis scheme (Barnes 1964; Trapp and Doswell 2000; Majcen et al. 2008). Following the suggestions of Pauley and Wu (1990), a smoothing parameter of $\kappa_0 = (1.33d)^2$ was used for the first pass, where d is the coarsest DOW data spacing in the analysis area. For the second pass, a smoothing parameter of $\kappa = 0.3\kappa_0$ was used, in accordance with the experiments of Majcen et al. (2008). Data spacing increased with altitude (in addition to range) owing to the DOW scanning strategy, which had larger differences in elevation angle between successive scans for elevation angles greater than 6.0° (e.g., there is only a 1.0° difference in the vertical between the sweeps at lower elevation angles, but a 2.0° difference between the higher sweeps; see Table 3). The low-level mesocyclone, rear-flank downdraft (RFD), and southern portion of the forward-flank downdraft (FFD) of the Prospect Valley storm were all within 14.35 km of both DOWs between 2225 and 2245 UTC. Therefore, we set $d = 14.35\,\text{km} \times (2.0°) \times (\pi/180°) = 0.501\,\text{km}$ and $\kappa_0 = (1.33 \times d)^2 = 0.444\,\text{km}^2$. A beamwidth of 2.0° was used to compute d because of the greater difference in elevation angle between successive DOW scans above 6.0°.

The grid spacing (Δx) was chosen to be between $d/3$ and $d/2$, as was done in Koch et al. (1983). The $z = 0$ km level of the Cartesian grid was chosen to correspond to the elevation of DOW7, because it was lower in elevation than DOW6. The mean storm motion from 2225 to 2245 UTC was approximated using the mean hook echo motion, which was subjectively determined to be (4.45, 3.51) m s^{-1} by following the hook echo stem in the DOW reflectivity fields (Fig. 3). In addition to using the mean storm motion to translate the grid, the mean storm motion was also used in a time-to-space conversion to move features within the various radar scans in a single volume to the correct storm-relative position. This procedure helped to remove the artificial tilt of storm features with height within a volume that results from the slightly different times that different elevation angles are scanned.

Parameters and details of the Barnes objective analysis are presented in Table 4 and the theoretical response function is presented in Fig. 4. Table 4 also defines the region where the radar data spacing is ≤0.501 km and the Barnes objective analysis can, therefore, be trusted. Owing to the close proximity of the DOWs to the low-level mesocyclone (Fig. 3), there is an abundance of radar observations near the mesocyclone (range ≤ 14 km) and below 1 km AGL, but very few observations above 1 km AGL.

The final step to obtain a three-dimensional wind field was to perform a dual-Doppler wind synthesis. This procedure only used the gridded DOW radial velocities within the

[4] The formation of a vortex like an SCV or tornado can occur in less than a minute, which makes a temporal resolution of 2 min too coarse to actually resolve the process of tornadogenesis. Instead, this study aims to describe the overall circumstances that prevented SCV 5 from further intensifying that have temporal scales greater than 2 min.

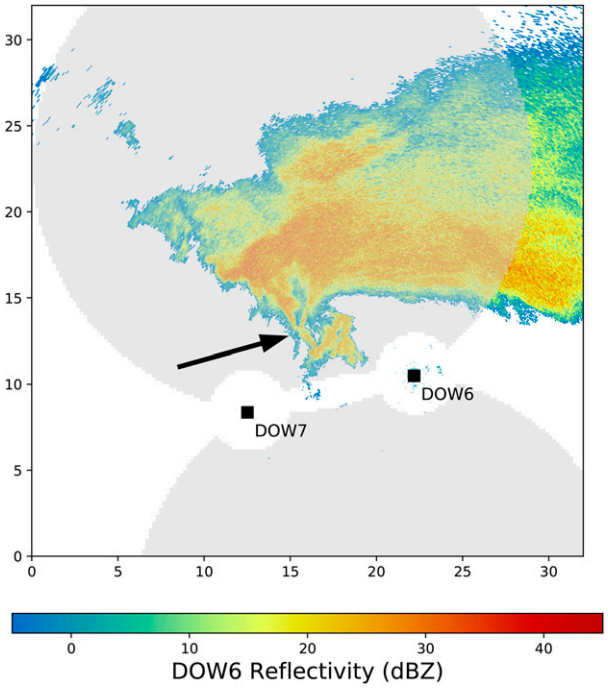

FIG. 3. DOW6–DOW7 dual-Doppler lobe (gray shading) overlaid on raw, uncalibrated DOW6 reflectivity (color shading) at 2236 UTC. The position of DOW6 and DOW7 are shown with the black squares and the black arrow indicates the hook echo stem. Axis labels are in km.

dual-Doppler lobe (Fig. 3), which is the region where the angle between the radar beams is within 20°–160°. The three components of the wind were computed iteratively at each vertical grid level via an upward integration of the mass continuity equation (Dowell and Shapiro 2003). As a boundary condition for this integration, vertical velocities were set to $0\,\mathrm{m\,s^{-1}}$ at the lowest grid level. Horizontal winds were extrapolated downward from the lowest level with data to the lowest grid level during integration by assuming that the vertical gradient of the dual-Doppler coefficients (e.g., Dowell and Shapiro 2003) was zero over the extrapolation depth. The downward-extrapolated winds were set to missing in the final dual-Doppler wind synthesis[5] and no downward extrapolation of horizontal winds occurred during integration if the lowest data level with horizontal winds was above 1.4 km AGL. This is a rather large depth to extrapolate horizontal winds downward, but owing to the abundance of DOW data in the lowest kilometer AGL, horizontal winds rarely had to be extrapolated downward over a depth greater than 0.4 km. No horizontal extrapolation of winds was permitted during integration or gridding.

[5] Although the winds at the lowest grid level were set to missing in the final dual-Doppler wind synthesis, wind data from aloft was again extrapolated to the lowest grid level in order to compute parcel trajectories. This was the only other time winds were extrapolated below radar level.

TABLE 4. Parameters for the Barnes objective analyses used for the Prospect Valley storm: d is the coarsest data spacing (vertical, in this case), κ_0 is the Barnes smoothing parameter, γ is the convergence parameter, Δx is the grid spacing, and φ is the radar elevation angle.

d (km)	0.501
κ_0 (km^2)	0.444
γ (unitless)	0.3
Δx (km)	0.20
Distance from either DOW where radar data spacing = d for $\varphi > 6.0°$ (km)	14.35
Distance from either DOW where radar data spacing = d for $\varphi \leq 6.0°$ (km)	28.71
Vertical Depth (km)	2.00
Data Horizon at 14 km from both DOWs (km AGL)	0.122

The impact of hydrometeor fall speeds on the radial velocities was ignored during the dual-Doppler synthesis owing to the difficulty in determining hydrometeor fall speeds from uncalibrated DOW reflectivities (e.g., Markowski et al. 2012a). Root-mean-square differences between one dual-Doppler wind synthesis that neglected hydrometeor fall speeds and another that used a hydrometeor fall speed of $10\,\mathrm{m\,s^{-1}}$ anywhere the DOW reflectivity exceeded 10.0 dBZ were less than $1\,\mathrm{m\,s^{-1}}$, with larger errors occurring near the edges of the dual-Doppler lobes and in regions of high reflectivity. This suggests that neglecting hydrometeor fall speeds alters the retrieved three-dimensional wind values, but not the qualitative character of the dual-Doppler wind synthesis. After assigning a three-dimensional wind vector to each grid point, the mean storm motion was subtracted to yield storm-relative winds.

The dual-Doppler wind syntheses from the Prospect Valley storm were used to compute parcel trajectories. To compute trajectories, winds from the dual-Doppler wind syntheses were first temporally interpolated between the dual-Doppler wind syntheses to increase the temporal resolution of the wind data from 2 min to 10 s (10 s was the time step used to compute the parcel trajectories). Next, the temporally interpolated winds were spatially interpolated to each parcel location. Finally, the parcel locations were advanced forward one time step using a fourth-order Runge–Kutta scheme. Sensitivity tests using time steps of 20 and 2 s demonstrate that the qualitative results of the parcel trajectories were insensitive to the time step used (not shown). While computing parcel trajectories, winds were extrapolated from the lowest grid level without missing data to the surface assuming a log-wind profile, following Markowski et al. (2012b), and were interpolated in regions of missing data using a Leise (1982) hole-filling algorithm.

The dual-Doppler wind syntheses also were used to perform a perturbation pressure (p') retrieval as in

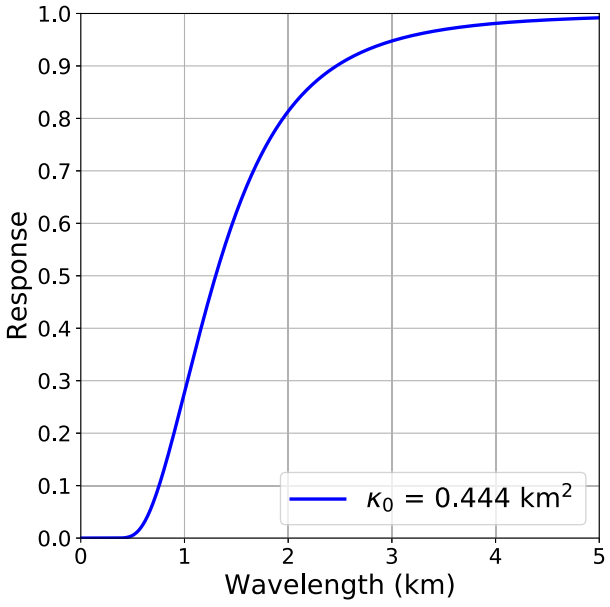

FIG. 4. Theoretical two-pass Barnes objective analysis response function for $\kappa_0 = 0.444\,\text{km}^2$. κ_0 is reduced to 30% of its original value (i.e., $0.1332\,\text{km}^2$) during the second pass.

Markowski et al. (2012b, 2018). The p' retrieval technique follows Gal-Chen (1978) and Hane and Ray (1985) and determines the pressure, up to an arbitrary constant, at each altitude. Because the retrieved p' values are used to qualitatively explore the horizontal pressure gradient acceleration (HPGA) field, the arbitrary constant is not a concern because it vanishes when computing horizontal gradients. To minimize errors in the retrieved p' field, retrievals were only attempted within subdomains where there was little missing data (<10% of the grid points had missing winds). Sensitivity tests showed that the qualitative representation of the p' field was insensitive to small changes in the boundaries of these subdomains.

b. *Mobile mesonet and mobile sounding data processing*

Near-surface temperature, relative humidity, pressure, wind speed, and wind direction measurements were collected at 1-s intervals by five mobile mesonet probes similar to those described by Straka et al. (1996). Quality control of mobile mesonet observations followed Markowski et al. (2002, 2012a), with the exception that temperature and relative humidity data collected while the probes were stationary were not removed for the Prospect Valley storm. Stationary thermodynamic measurements were retained for this case owing to the increased aspiration of the temperature sensors in the mobile mesonet that came with using "U-tubes" in the 2010 field phase of VORTEX2 compared to the "J-tubes" used in 2009 (Waugh and Fredrickson 2010; Klees et al. 2016). Additional information about the instrumentation of the mobile mesonet and errors associated with these measurements can be found in Straka et al. (1996) or Markowski et al. (2002).

After quality control, mobile mesonet observations were smoothed using two passes of a triangular filter with a radius of five seconds (e.g., Shabbott and Markowski 2006; Markowski et al. 2012a). Smoothed mobile mesonet observations were then plotted in a storm-relative reference frame by employing a time-to-space conversion that utilized the same mean storm motion that was used in the radar gridding and dual-Doppler wind synthesis (Markowski et al. 2002). Plots of mobile mesonet observations relative to the Prospect Valley storm were created using a 4-min window (i.e., mobile mesonet observations from 2 min prior to and 2 min after the analysis time were plotted) in order to minimize the errors arising from the time-to-space conversion.

For better comparison to the studies of Markowski et al. (2002) and Grzych et al. (2007), perturbation virtual and equivalent potential temperatures were computed using mobile mesonet data. To determine perturbation values, a base state needed to be defined. Similar to Skinner et al. (2014) and Klees et al. (2016), a 20-min average across all mobile mesonet probes prior to the mesonet intercepting the Prospect Valley storm between 2105 and 2125 UTC was used to determine the base state owing to the relatively constant values of thermodynamic quantities across all probes during this period (not shown). Owing to the different formulation of the base state used in this study compared to Markowski et al. (2002) and Grzych et al. (2007), care should be used when comparing numeric values of perturbations between the aforementioned studies and the Prospect Valley storm.

The NSSL1 MGAUS launched at 2223:46 UTC was selected as the inflow sounding because it was launched immediately before the period of interest and was located southeast of the Prospect Valley storm (i.e., the environmental inflow region; Fig. 2). MGAUS data were quality controlled following the methods discussed by Parker (2014). Similar to Parker (2014) and Klees et al. (2016), MGAUS wind measurements were interpolated onto a 0.050 km vertical grid using a one-pass Barnes objective analysis with a smoothing parameter of $\kappa = 2.5 \times 10^{-3}\,\text{km}^2$. Unlike Klees et al. (2016), the same value of κ was used for the entire vertical depth of the sounding. SRH and bulk wind differences were computed using the smoothed wind fields.

3. Observations: 2225–2245 UTC

The Prospect Valley storm lasted from about 1845 UTC 26 May 2010 to about 0215 UTC 27 May 2010, but we will focus on the 2225–2245 UTC time period because there

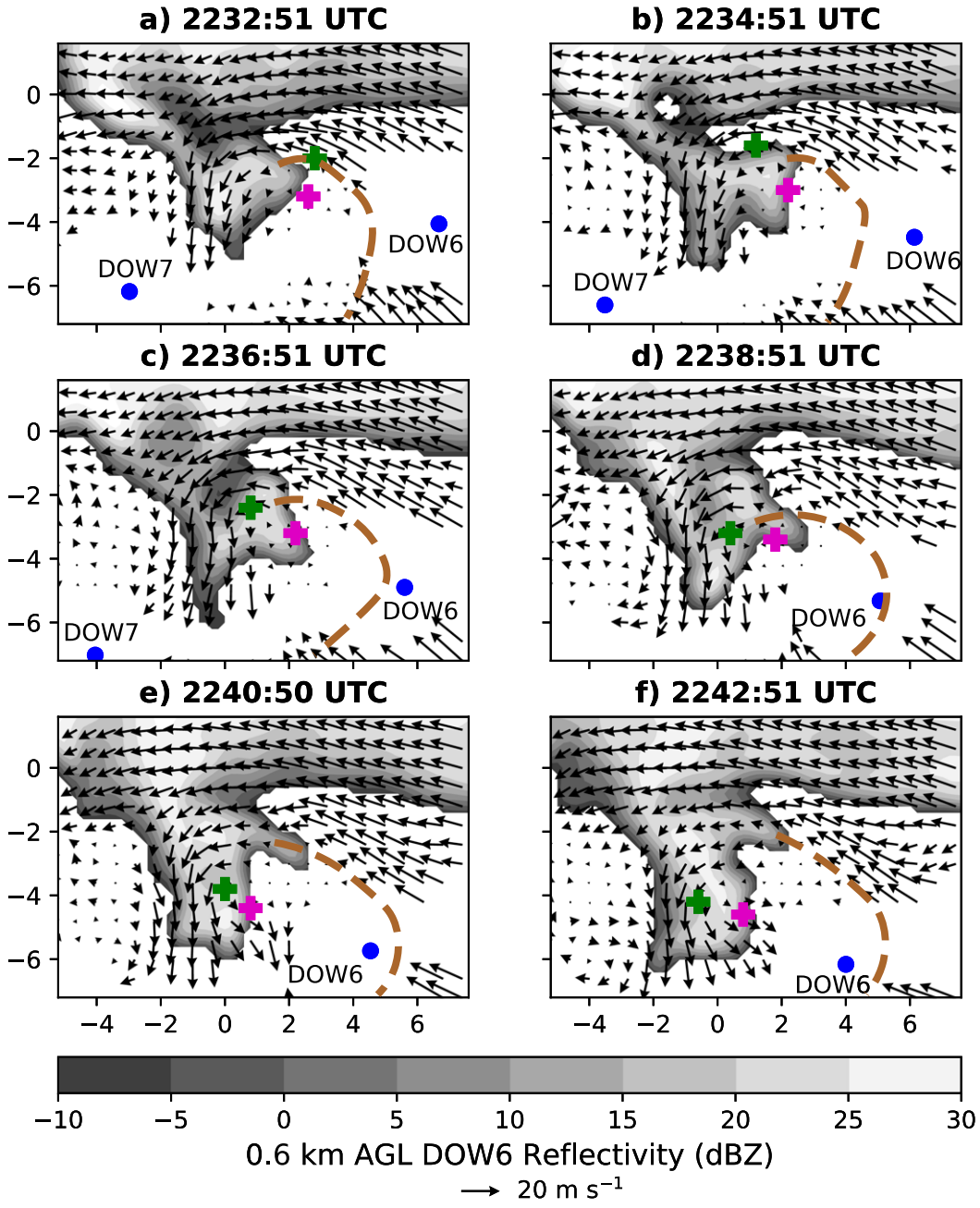

FIG. 5. Gridded DOW6 reflectivity and dual-Doppler wind synthesis horizontal wind vectors (every third vector) at 0.6 km AGL at (a) 2232:51, (b) 2234:51, (c) 2236:51, (d) 2238:51, (e) 2240:50, and (f) 2242:51 UTC. The green crosses, magenta crosses, blue dots, and dashed brown lines represent the locations of the 0.6 km AGL Okubo–Weiss number minimum, 0.6 km AGL 2-km-radius circulation maximum, DOWs, and rear-flank gust front, respectively. Gust front positions are subjectively determined using mobile mesonet observations and 0.2 km AGL dual-Doppler winds. Axis labels are in km.

were good dual-Doppler and mobile mesonet observations during this time. During this time period, the Prospect Valley storm had a well-defined hook echo that coincided with an area of broad circulation (Fig. 5), which is associated with a maximum in the circulation field computed using circuits with a radius of 2 km centered on each grid point (hereafter the 2-km-radius circulation). These maxima in 2-km-radius circulation are used to identify the low-level mesocyclone center (magenta crosses in Fig. 5), though it is worth noting that

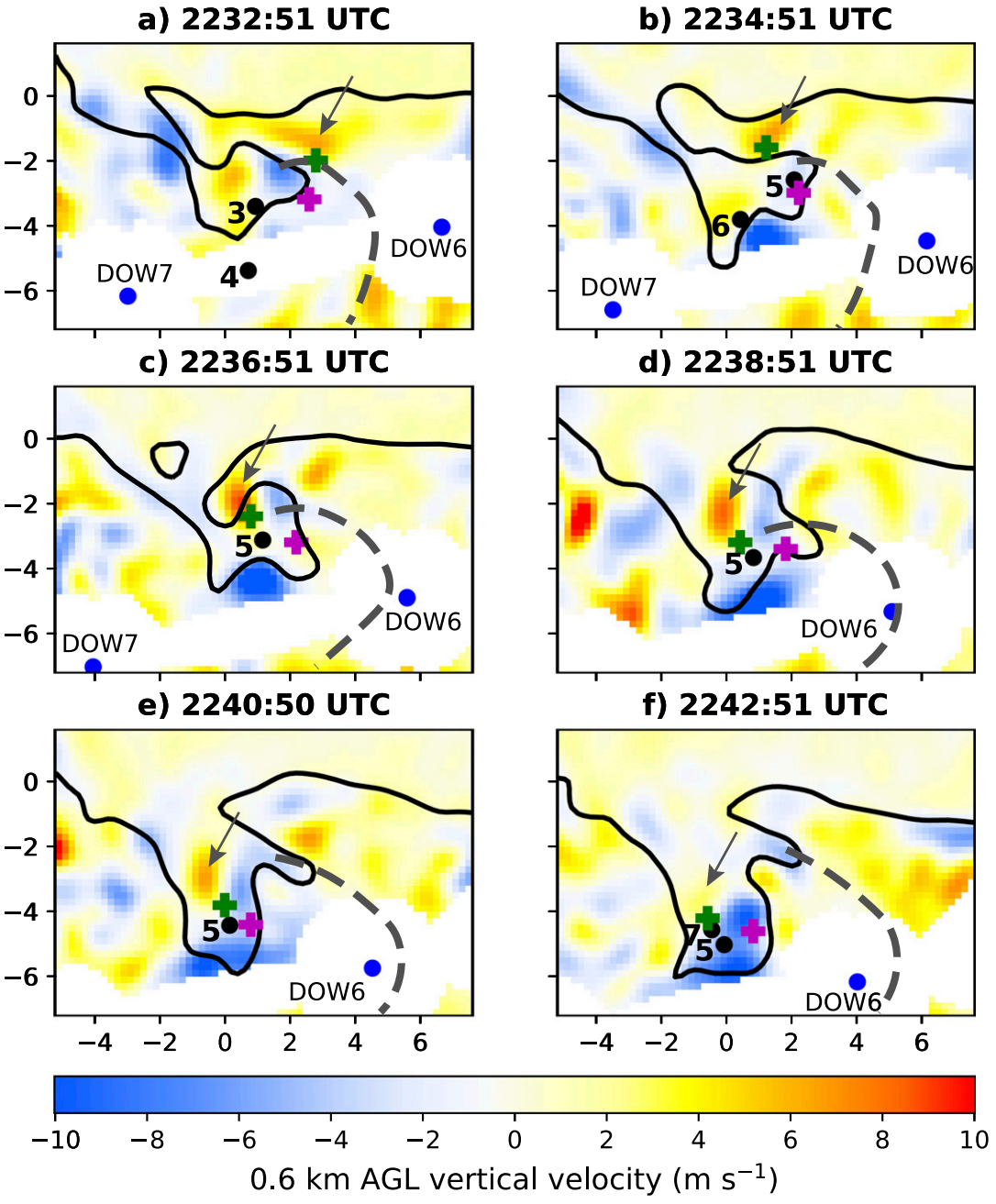

FIG. 6. The 0.6 km AGL vertical velocity field (color shading) and 0.4 km AGL 15-dBZ reflectivity contour (heavy black contour) at (a) 2232:51, (b) 2234:51, (c) 2236:51, (d) 2238:51, (e) 2240:50, and (f) 2242:51 UTC. The green crosses, magenta crosses, black dots, blue dots, and dashed gray lines represent the locations of the 0.6 km AGL Okubo–Weiss number minimum, 0.6 km AGL 2-km-radius circulation maximum, SCVs, DOWs, and rear-flank gust front, respectively. SCV locations come from Tanamachi et al. (2013) using the UMass W-band radar. Gray arrows denote the updraft pulse discussed in the text. Axis labels are in km.

the 2-km-radius circulation maxima in Figs. 5e and 5f appear to be shifted to the southwest of the low-level mesocyclone center based on a subjective analysis of the horizontal wind field. Regardless, the broad rotation associated with the low-level mesocyclone appears rather steady over the 2225–2245 UTC time period (Fig. 5). A distinct wind shift associated with the rear-flank gust front is also evident at multiple times within the wind field east of the hook echo (e.g., (4, −3) in Figs. 5a and 6a). Interestingly, SCV 5 appears to develop close to the

rear-flank gust front (Fig. 6b), then moves farther away from the rear-flank gust front later in the time period (e.g., Fig. 6e). It is possible that the displacement of SCV 5 from the convergence associated with the gust front (which was likely important for its genesis) may have contributed to its demise later in this period.

An interesting kinematic feature of the Prospect Valley storm during the 2225–2245 UTC time period is the development of an updraft pulse and minimum in the Okubo–Weiss number (OW; Okubo 1970; Weiss 1991; Markowski et al. 2011) along the edge of the low-level mesocyclone (green crosses in Figs. 5 and 6). OW is defined as $\mathrm{OW} = D^2 - \zeta^2$, where D is the total deformation, and is typically used to diagnose regions of rotation (OW minima) and deformation (OW maxima). A region of negative OW developed east of the 2-km-radius circulation in a region of updraft along the rear-flank gust front at 2230 UTC (not shown) and then intensified as it was advected cyclonically around the 2-km-radius circulation maximum over the next three time steps (Figs. 5a–c and 7a–c). During the same time period, an updraft pulse (gray arrows in Fig. 6) also intensified and was advected cyclonically by the low-level mesocyclone. The updraft pulse reached its peak intensity at 2236:51 UTC (Fig. 6c), which coincided with the peak intensity of SCV 5 and led the peak intensity of the OW minimum by 2 min (Fig. 7d). At these times, the OW minimum was located on the interface between the updraft pulse to the west and a downdraft to the east (Figs. 7c,d). After 2238:51 UTC, the OW minimum and updraft pulse weakened and continued to move rearward within the storm (Figs. 7e,f and 6e,f) and eventually dissipated at 2244:51 UTC (not shown).

The overall character of the vertical velocity field in the Prospect Valley storm is similar to what might be expected in a nontornadic or weakly tornadic storm. As shown in Fig. 6, the vertical velocity field is rather unsteady and is similar to that of the nontornadic simulation of Coffer and Parker (2017), with interspersed pockets of updraft and downdraft throughout the hook echo region [e.g., the downdraft near (1.5, −2) in Fig. 6c and the updraft pulse noted earlier]. Focusing specifically on SCV 5, time-height cross sections of vertical velocity and convergence show that the column of air directly above SCV 5 is characterized primarily by meso-γ-scale divergence and vertical velocities that are either negative (~2235:00 and 2240:00–2243:53 UTC in Fig. 8) or near-zero. Both the unsteadiness of the vertical velocity field and the location of SCV 5 in a region not conducive for positive vertical vorticity stretching likely prevented the development of a significant tornado during the analysis period.

Mobile mesonet virtual potential temperature perturbations (θ_v') during this time period are shown in Fig. 9. The utility of examining θ_v' is that it is a proxy for parcel buoyancy if the impacts of hydrometeor loading are ignored. The θ_v' values sampled by the mobile mesonet west of the low-level mesocyclone center near (−1.0, −5.0) at 2234:51 and 2238:51 UTC are between −2 and −3 K, whereas values northwest of the mesocyclone center near (−2.0, −3.0) are closer to −5 and −6 K (Figs. 9b,c). This indicates that there is an appreciable amount of heterogeneity in the buoyancy characteristics of the RFO in the Prospect Valley storm, with some parts of the RFO possessing air parcels that are more negatively buoyant than others. The impact of this heterogeneity on the inability for a strong tornado to form is discussed more in section 4.

Another interesting characteristic of the mobile mesonet observations is a pocket of near-zero θ_v' deficits in the vicinity of a strong downdraft on the southern tip of the hook echo near (1.0, −4.5) at 2234:51 and (1.0, −5.5) at 2238:51 UTC (Figs. 9b,c and 6b–e). This downdraft can be seen more clearly in a 4-min analysis centered at 2236:51 UTC (Fig. 10a). Diffluence in the mobile mesonet winds and strong divergence in the 0.2 km AGL dual-Doppler wind syntheses also is observed in this region. Because equivalent potential temperature (θ_e) is approximately conserved in moist processes,[6] it can be used as a tracer to determine the origin of air parcels. The θ_e' values near −1 K in the vicinity of the downdraft (hereafter the "warm downdraft" because the parcels composing the downdraft are relatively warmer than the rest of the RFO) indicate that these air parcels may have origins in the near-storm inflow close to the surface (Fig. 10). The larger θ_e' deficits outside of the warm downdraft within the RFO suggests that parcels within the rest of the RFO have parcel origins from farther aloft, which differs from the warm downdraft. The potential role of the warm downdraft on the evolution of SCV 5 will be explored in section 6.

4. Comparison to the tornadic Goshen County, Wyoming, storm

This section uses azimuthally averaged fields in a manner similar to Markowski et al. (2011) to compare

[6] The values of θ_e computed in this article are pseudoequivalent potential temperatures and are not strictly conserved for moist processes, because when calculating the pseudoequivalent potential tempertaure, it is assumed that any condensate that forms is immediately removed from the parcel. Therefore, the influences of freezing and melting as well as temperature changes of the condenstate are not accounted for. The differences between equivalent potential temperature and pseudoequivalent potential temperature are small, so the latter is conserved, to a good approximation, in moist processes.

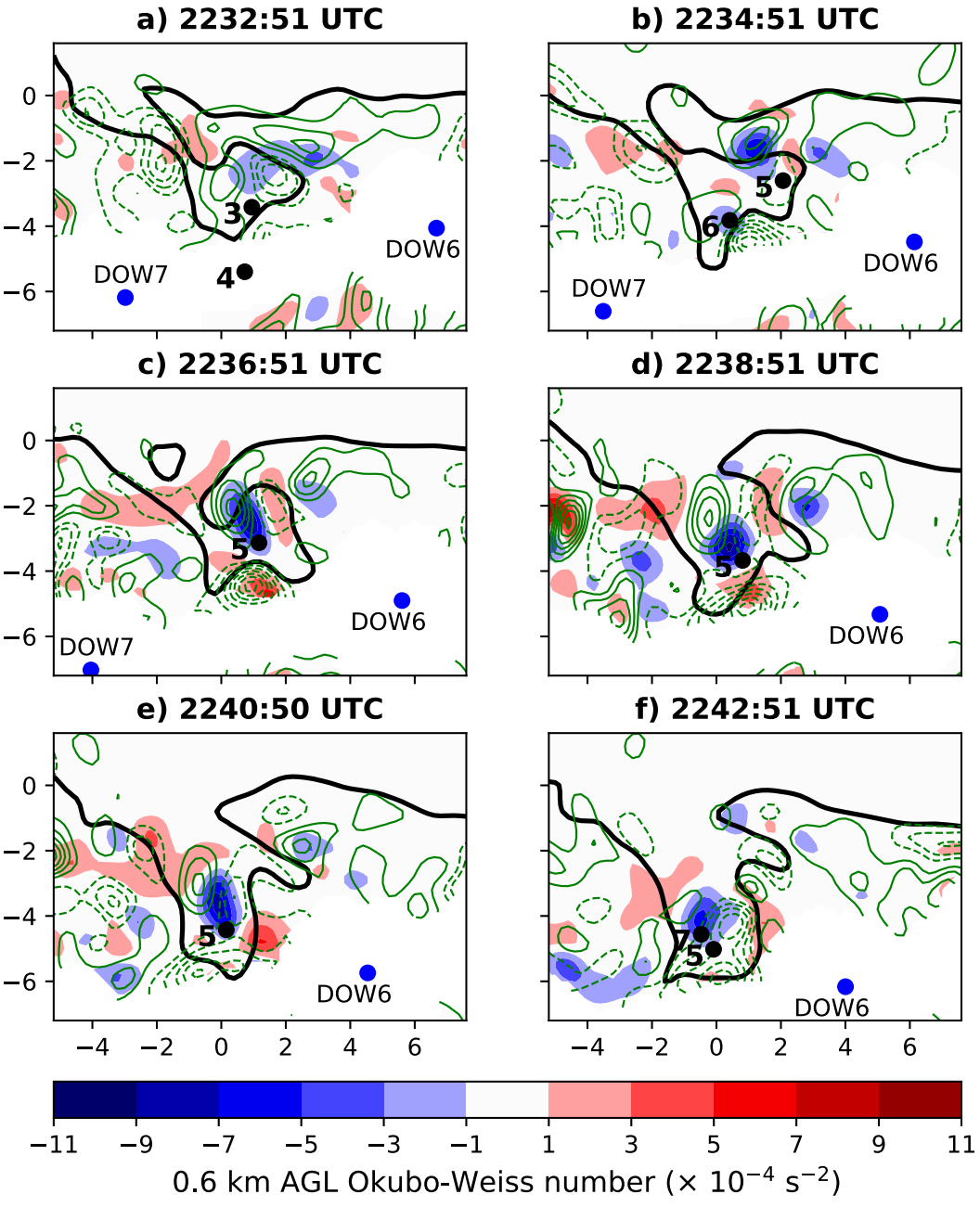

FIG. 7. The 0.6 km AGL Okubo–Weiss number (color shading), 0.6 km AGL 2 m s^{-1} vertical velocity contours (green; zero contour omitted, negative contours dashed), and 0.4 km AGL 15-dBZ reflectivity contour (heavy black contour) at (a) 2232:51, (b) 2234:51, (c) 2236:51, (d) 2238:51, (e) 2240:50, and (f) 2242:51 UTC. The blue and black dots represent the locations of the DOWs and SCVs, respectively. Axis labels are in km.

the Prospect Valley storm to the tornadic Goshen County, Wyoming, storm intercepted by VORTEX2 on 5 June 2009 (hereafter the Goshen County storm), which is one of the best-sampled tornadic storms from any field project to date (Markowski et al. 2012a). To better facilitate a comparison between the Prospect Valley and Goshen County storms, new dual-Doppler syntheses for the Prospect Valley storm were created using the same procedure and parameters outlined in section 2a except that the horizontal and vertical grid spacings were changed to 0.25 km and the Barnes smoothing parameter was changed to $\kappa_0 = 0.48\ \text{km}^2$ in order to match the gridding parameters used in the fine dual-Doppler syntheses for the pretornadic phase of the

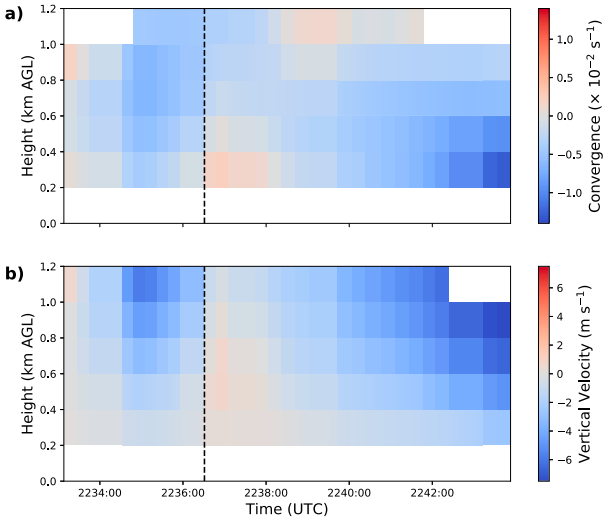

FIG. 8. Time–height profiles of dual-Doppler (a) convergence and (b) vertical velocity at the location of SCV 5 from 2233:08 to 2243:53 UTC (color shading). The dashed, black line indicates the time when SCV 5 was strongest in the UMass W-band observations (Tanamachi et al. 2013).

Goshen County storm (see section 2a of Markowski et al. 2012a). It is worth noting that this comparison is particularly useful because these storms formed in environments with similar values of low-level SRH [the environment of the Goshen County storm only had 88 $m^2 s^{-2}$ of 0–1 km SRH (Markowski et al. 2012a), which is comparable to that of the Prospect Valley storm] and similar geographic regions (northeast Colorado and southeast Wyoming), and they were observed using nearly the same instruments (barring small improvements to VORTEX2 assets from 2009 to 2010).

To assess the circulation available within the Prospect Valley and Goshen County storms for the low-level mesocyclone, radial circulation profiles were constructed using the maximum of the 2-km-radius circulation field as the low-level mesocyclone center (Fig. 11). Surprisingly, the Prospect Valley storm had slightly more circulation in the far-field (radii > 2.25 km) than the Goshen County storm, even though the Prospect Valley storm only produced an SCV that lasted about 10 min and the Goshen County storm produced a tornado that lasted almost 40 min and peaked at EF2 intensity (Markowski et al. 2012a). Stark differences between the two circulation profiles can be seen closer to the low-level mesocyclone center, with the Prospect Valley storm displaying very little circulation at radii between 0 and 0.5 km (owing to weak horizontal winds close to the 2-km-radius circulation maximum, see Fig. 5b) and the Goshen County storm exhibiting circulation values approximately three times that of the Prospect Valley storm at a radius of 1 km. An additional comparison between the circulation profile of the Prospect Valley storm and Fig. 15 from Markowski et al. (2018) illustrates that the Prospect Valley storm also possessed substantially less circulation than the tornadic 12 May 2010 supercell near Clinton, Oklahoma, at all times for radii less than 1.0 km, but the Prospect Valley storm had similar circulation values for radii greater than 1.5 km. These two comparisons suggest that similarly effective circulation generation mechanisms were present in the Prospect Valley storm as in these two tornadic supercells (because the far-field circulation values were comparable), but that the circulation in the Prospect Valley storm was acted upon by weaker horizontal convergence relative to the tornadic cases.

The conclusion that the Prospect Valley storm was unable to converge far-field circulation is corroborated by the time-radius plots in Fig. 12. These plots show predominantly positive or near-zero azimuthally averaged radial velocities at all radii (indicating flow diverging from the circuit) as well as mostly negative or near-zero azimuthally averaged vertical velocities at radii up to 1.5 km for the Prospect Valley storm. This lack of inward and upward motion close to the low-level mesocyclone center in the Prospect Valley storm inhibits the convergence of the far-field circulation to smaller radii (Fig. 12e). In contrast, the Goshen County storm exhibits mostly negative azimuthally averaged radial velocities and positive azimuthally averaged vertical velocities (Figs. 12b,d), which results in a steady increase in circulation at all radii with time (Fig. 12f). These results are similar to the conclusions of Markowski et al. (2011, 2012a, 2018) that the inability for the low-level mesocyclone to converge far-field circulation is one potential mode of tornadogenesis failure.

In an attempt to determine why the Prospect Valley storm is unable to converge far-field circulation to radii less than 1 km, a proxy for the "forcing" of the dynamic perturbation pressure gradient is examined. This is done by computing the negative vertical gradient of $\mathrm{OW} + \delta^2$, where δ is the horizontal divergence, for both the Prospect Valley and Goshen County storms using centered finite differences (Figs. 13a,b). The utility of examining $\mathrm{OW} + \delta^2$ is that it is equal to the dynamic terms of the diagnostic p' equation that involve horizontal gradients of horizontal winds (section 2.5.3, Markowski and Richardson 2010). Therefore, $-\partial(\mathrm{OW} + \delta^2)/\partial z$ is a proxy for the dynamic VPPGF that results from horizontal winds.[7] Ideally, $-\partial[\nabla \cdot (\mathbf{v} \cdot \nabla \mathbf{v})]/\partial z$ should be

[7] Even if the horizontal gradients of the horizontal winds are all that contributes to the dynamic p', $-\partial(\mathrm{OW} + \delta^2)/\partial z$ is still only a proxy for the dynamic VPPGF (and is not necessarily proportional to the dynamic VPPGF) owing to the assumption that $\nabla^2 p' \propto -p'$ is made for each vertical level.

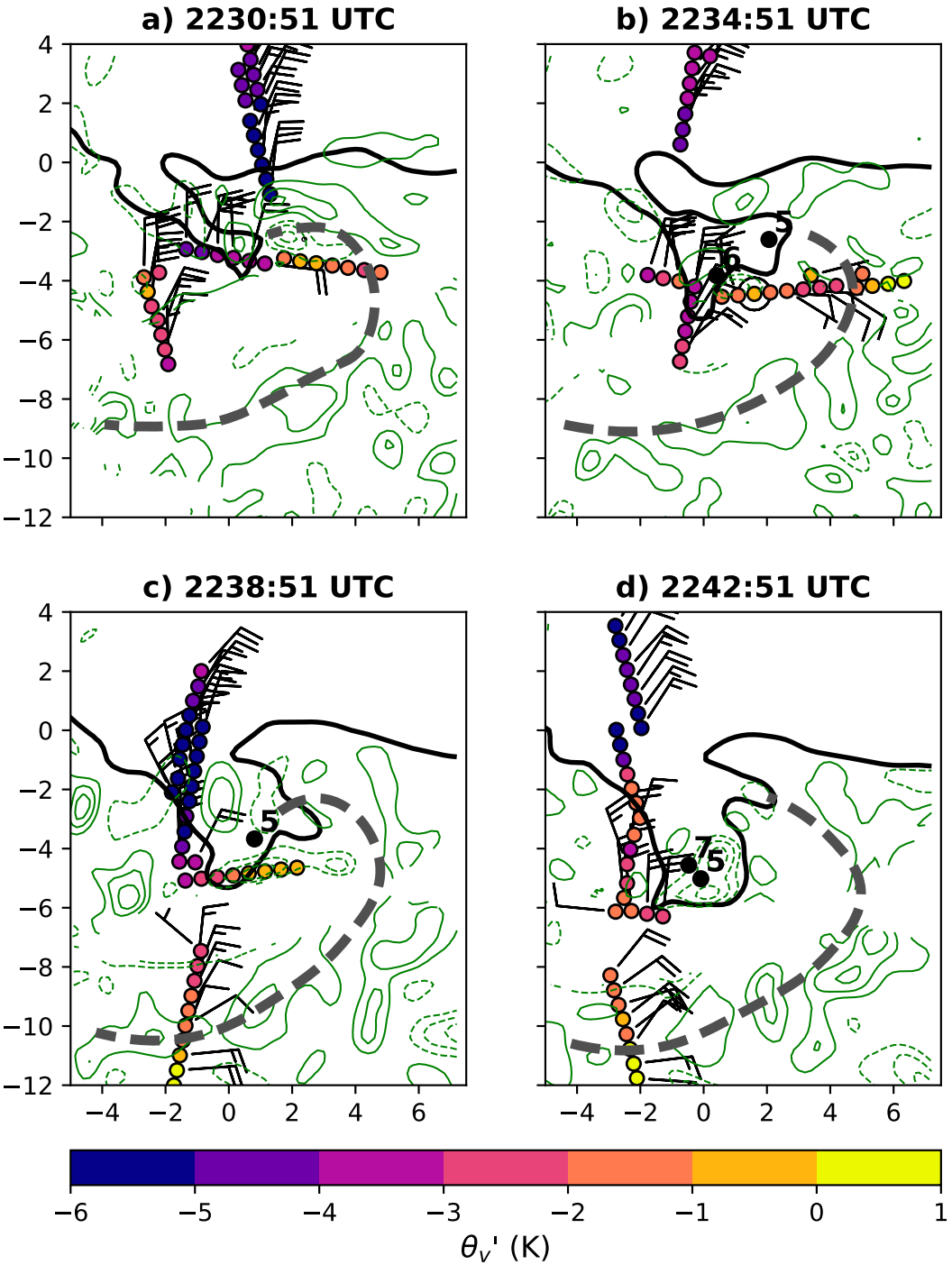

FIG. 9. Time-to-space converted mobile mesonet plots of perturbation virtual potential temperature (color shading) and storm-relative winds (barbs; full barb represents 5 m s^{-1}, half barb represents 2.5 m s^{-1}) at (a) 2230:51, (b) 2234:51, (c) 2238:51, and (d) 2242:51 UTC. Dual-Doppler wind synthesis 0.2 km AGL convergence values are plotted with green contours (every 0.005 s^{-1}; zero contour omitted, negative contours dashed), gust fronts are represented with dashed gray lines, and the heavy black contour represents the 0.4 km AGL 15-dBZ outline. Black dots represent the locations of the SCVs. Axis labels are in km.

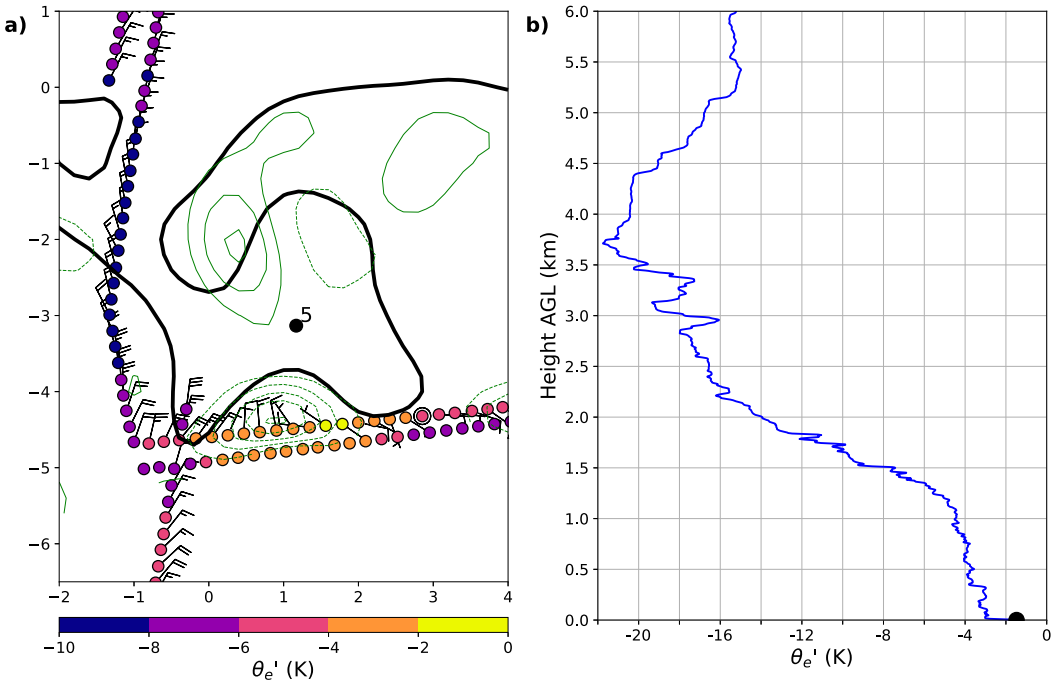

FIG. 10. Equivalent potential temperature structure in the hook echo region and environment. (a) As in Fig. 9, but at 2236:51 UTC and with equivalent potential temperature perturbations plotted instead of virtual potential temperature perturbations. (b) Equivalent potential temperature perturbation trace from the 2223 UTC NSSL1 MGAUS with the black semicircle representing the surface value. Equivalent potential temperature perturbations in (b) were computed by taking θ_e from the sounding and subtracting the θ_e value from the mobile mesonet thermodynamic base state (the base state θ_e value is 341.9 K).

plotted to get a more representative proxy of the dynamic VPPGF, but this field is more prone to error owing to the additional finite differences in the vertical that are needed and the relatively coarse vertical grid spacing of the dual-Doppler wind syntheses.

Not surprisingly, the maximum in $-\partial(\mathrm{OW} + \delta^2)/\partial z$ is nearly collocated with the minimum in OW for both storms. What is surprising is that $-\partial(\mathrm{OW} + \delta^2)/\partial z$ is actually larger for the Prospect Valley storm, which suggests that the Prospect Valley storm has a larger upward-directed dynamic VPPGF than the Goshen County storm. So why was the far-field circulation converged to smaller radii in the Goshen County storm? An examination of the 0.5 km AGL vertical velocity field reveals that the two storms exhibit comparable vertical velocities in the vicinity of the $-\partial(\mathrm{OW} + \delta^2)/\partial z$ maximum (Figs. 13c,d). Noting that dw/dt scales as W^2/D, where W is the vertical velocity scale and D is the depth scale, the observation that the vertical velocities are comparable suggests that dw/dt is comparable between the two storms. The two primary forcing terms for dw/dt are the dynamic VPPGF and the effective buoyancy (Doswell and Markowski 2004). Therefore, if the VPPGF is larger in the Prospect Valley storm, but dw/dt is comparable between the two storms, the effective buoyancy forcing must be greater in the Goshen County storm.

The conclusion that the effective buoyancy is larger in the Goshen County storm than the Prospect Valley storm is supported by mobile mesonet observations from both storms. The Prospect Valley storm possessed some θ_v' values near -5 and -6 K within 2 km of the $-\partial(\mathrm{OW} + \delta^2)/\partial z$ maximum (Fig. 9) whereas θ_v' values in the Goshen County storm are generally ≥ -3 K within 2 km of the $-\partial(\mathrm{OW} + \delta^2)/\partial z$ maximum (Markowski et al. 2012a). Furthermore, LCLs computed using mobile mesonet observations within the inflow immediately east of the hook echo in both storms are lower in the Goshen County storm compared to the Prospect Valley storm (not shown). This indicates that the RFO in the Prospect Valley storm may have had a tendency to be (virtually) colder than the Goshen County storm owing to increased evaporational cooling (Rasmussen and Blanchard 1998; Markowski et al. 2002; Thompson et al. 2003). The presence of parcels with strong negative buoyancy in a portion of the RFO of the Prospect Valley storm likely contributed to the inability for circulation-rich parcels to be converged to small radii compared to the Goshen County storm despite the Prospect Valley storm possessing stronger forcing for

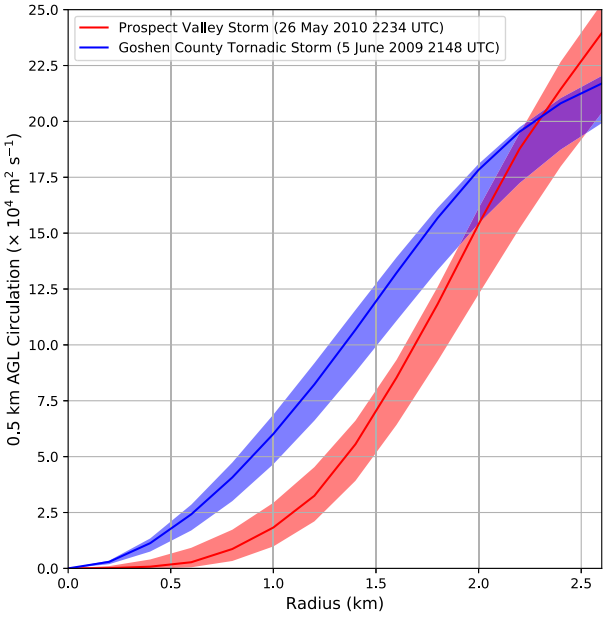

FIG. 11. Circulation as a function of radius (i.e., distance from the axis of rotation) for the Prospect Valley storm (red) 4 min prior to the Okubo–Weiss number temporal minimum at 0.5 km AGL and the tornadic 5 Jun 2009 Goshen County, WY, storm (blue) 4 min prior to tornadogenesis (Markowski et al. 2012a). The axis of rotation in both cases is the location of the 2-km-radius circulation maximum at 0.5 km AGL. The mean radial circulation profile from 1000 random perturbations of the circulation center ±1 standard deviation is shown with the shaded envelopes (perturbed circulation centers are generated using a Gaussian distribution centered on the location of the OW minimum with a standard deviation of 0.5 km). The circulation profile for the Prospect Valley storm is computed using the $\kappa_0 = 0.48\,\mathrm{km}^2$ dual-Doppler wind synthesis.

an upward dynamic VPPGF at low levels. This conclusion is similar to those from Markowski et al. (2002) and Grzych et al. (2007) that the likelihood of tornadogenesis decreases as the outflow becomes more negatively buoyant.

In addition to RFO buoyancy, the location of the OW minimum likely also contributed to the inability of the Prospect Valley storm to converge low-level circulation to smaller radii. The OW minimum, as well as the $-\partial(\mathrm{OW} + \delta^2)/\partial z$ maximum, is displaced from the 2-km-radius circulation maximum by ~2 km in the Prospect Valley storm, whereas this displacement is only ~1 km in the Goshen County storm (Figs. 13a,b). To converge far-field circulation toward the low-level mesocyclone center, the upward dynamic VPPGF should be located close to the center of rotation. Furthermore, the location of the OW minimum along the edge of the low-level mesocyclone in the Prospect Valley storm likely contributed to the OW minimum being advected rearward in the storm with time toward more negatively buoyant outflow, which further slowed upward accelerations and may have ultimately led to the demise of the updraft pulse associated with the OW minimum in the Prospect Valley storm. Thus, in addition to possessing a strong upward-directed dynamic VPPGF, a favorable location of the dynamic VPPGF also appears to be necessary to converge far-field circulation.

5. Low-level trajectory analysis

a. *Motivation*

The previous two sections have indicated that the Prospect Valley storm possessed a disorganized low-level vertical velocity field without a persistent low-level updraft and a weak low-level mesocyclone with relatively small circulation values close to the mesocyclone center. Recent modeling work has indicated that low-level updraft organization and low-level mesocyclone strength are related to the amount of near-storm environmental streamwise vorticity ingested by the supercell (e.g., Coffer and Parker 2017). The environment of the Prospect Valley storm possessed relatively little low-level streamwise vorticity (Table 2, Fig. 1), with only $40.3\,\mathrm{m}^2\,\mathrm{s}^{-2}$ of 0–500 m SRH, which is more similar to the median 0–500 m SRH in the nontornadic soundings examined by Coffer et al. (2019) than that for the weakly tornadic (EF0–1) soundings (63.69 and $126.81\,\mathrm{m}^2\,\mathrm{s}^{-2}$ for the nontornadic and weakly tornadic soundings, respectively). This suggests that the disorganization of the low-level updraft and weakness of the low-level mesocyclone close to the center of rotation may be in part a result of the storm ingesting parcels with little streamwise vorticity at low levels. To further test this hypothesis, this section examines the origins of parcels composing the OW minimum.

b. *OW minimum origins: Backward trajectory analysis*

A series of backward trajectories initiated in the vicinity of the OW minimum 0.6 km AGL at 2236:51 UTC is used to determine the origin of parcels contributing to the OW minimum (Fig. 14a). All trajectories use a time step of 10 s and are integrated backward in time for 15 min. Representative backward trajectories are presented in Fig. 15 with all resulting trajectories displayed in Fig. 14b. Vorticity vectors from the dual-Doppler wind syntheses are interpolated to the trajectories above 0.2 km AGL in order to evaluate the evolution of the three-dimensional vorticity along these trajectories before the parcels reach the OW minimum. Owing to the large fraction of parcel trajectories (35 out of 90) that spend >40% of their time below the dual-Doppler data horizon (0.2 km AGL) and the fact that the log-wind profile used below the data horizon is likely not

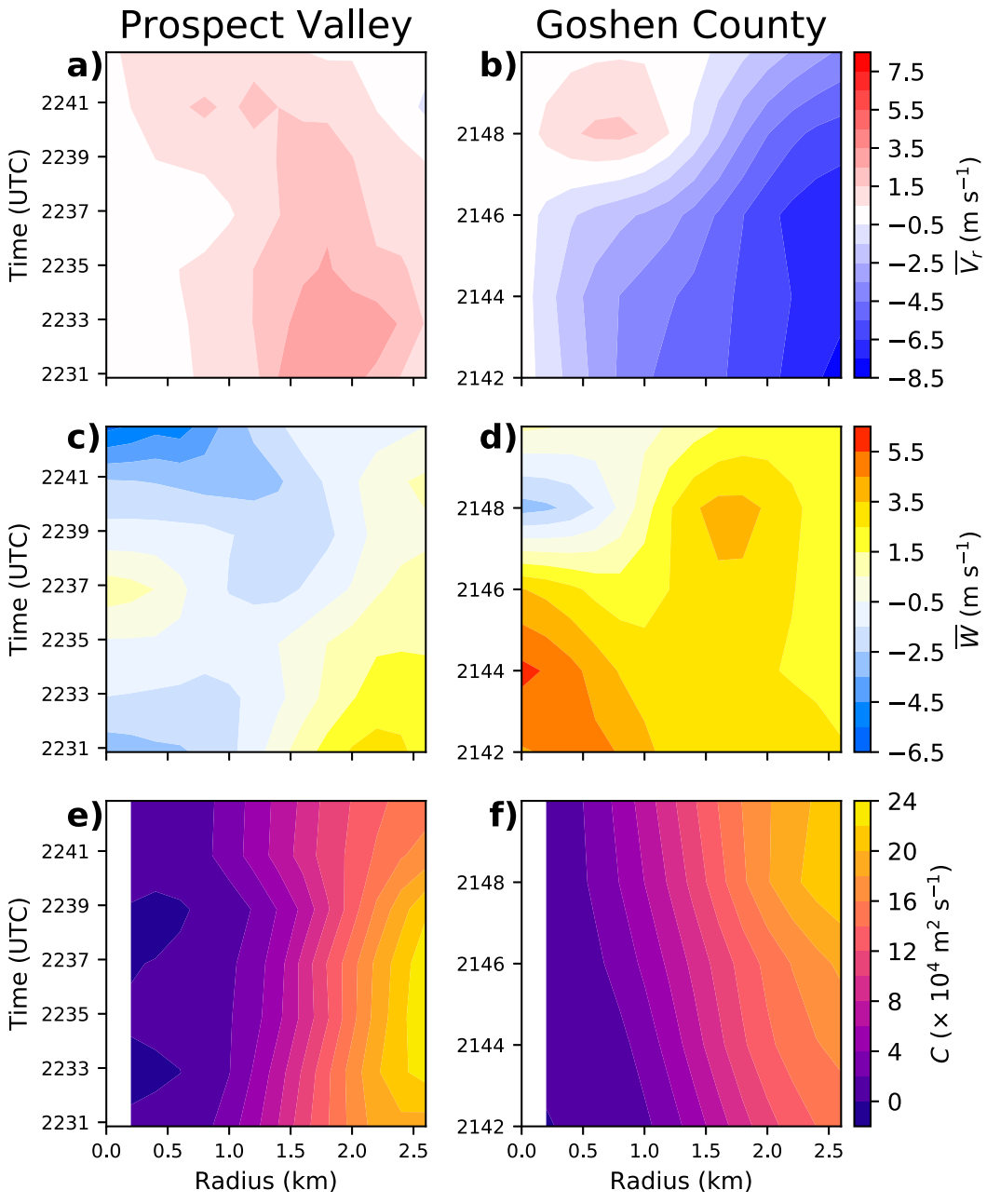

FIG. 12. Circuit radius vs time plots at 0.5 km AGL of (a),(b) azimuthally averaged radial velocity, (c),(d) azimuthally averaged vertical velocity, and (e),(f) circulation for circuits centered on the 2-km-radius circulation maximum at 0.5 km AGL in the Prospect Valley and Goshen County storms. Plots for the Prospect Valley storm are computed using the $\kappa_0 = 0.48\,\text{km}^2$ dual-Doppler wind syntheses.

appropriate for the surface layers of convective storms (e.g., Markowski et al. 2019), parcel trajectories in Figs. 14b and 16 are truncated where the parcels descend below 0.2 km AGL.

Many of the trajectories contributing to the OW minimum approach from the region east of the hook echo in the near-storm inflow south of the forward-flank reflectivity gradient (Fig. 14b). These trajectories support the theory mentioned in section 5a that near-storm environmental low-level shear and SRH are important for low-level mesocyclogenesis (e.g., Coffer and Parker 2017) due to the stretching and tilting of horizontal vorticity into the vertical along trajectories originating from the near-storm environment east of the hook echo. Before reaching the OW minimum, the vorticity along these trajectories is primarily weak and crosswise (Figs. 15c,d).

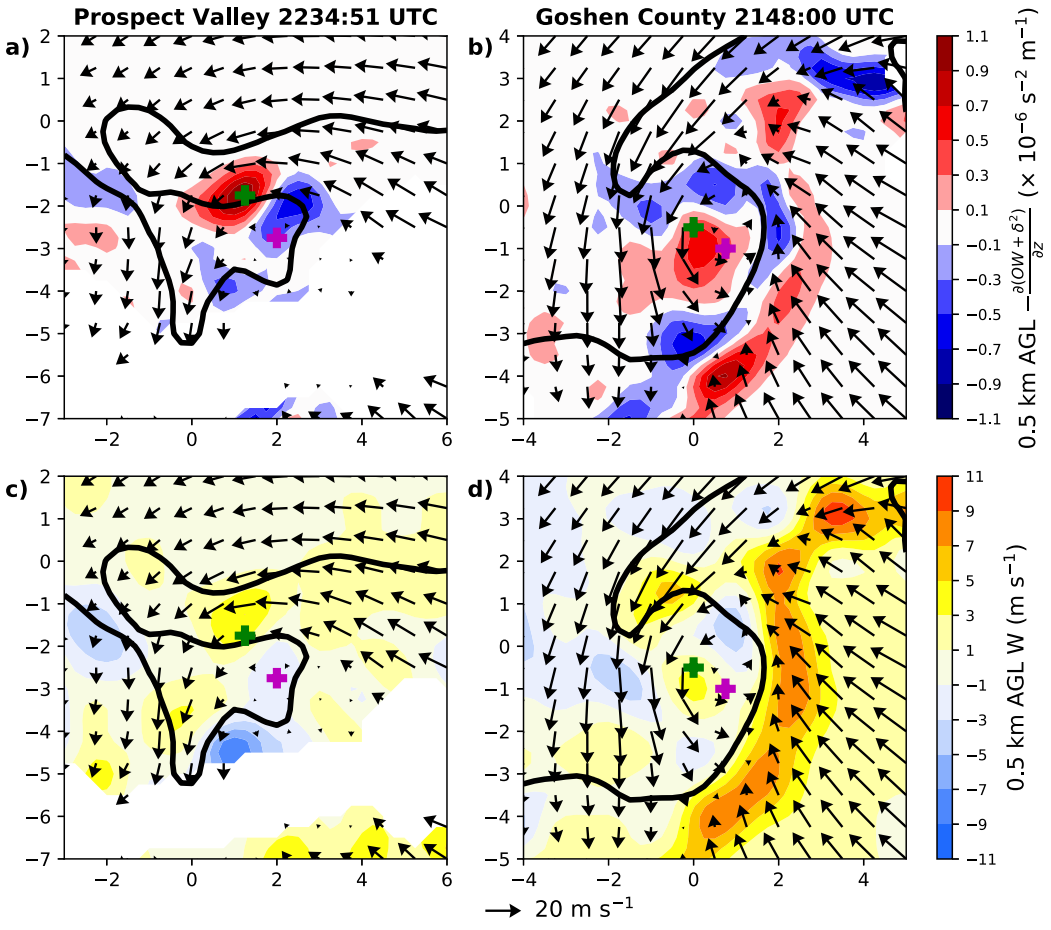

FIG. 13. Proxy for the "forcing" of the dynamic VPPGF. (a),(b) Negative vertical gradient of OW + δ^2 and (c),(d) the vertical velocity in the Prospect Valley storm at 2234:51 UTC and the Goshen County storm at 2148:00 UTC. Vectors represent the horizontal winds, heavy black contour represents the 15-dBZ reflectivity contour, and the green and magenta crosses represent the Okubo–Weiss number minimum and 2-km-radius circulation maximum, respectively. Plots for the Prospect Valley storm are computed using the $\kappa_0 = 0.48\,\text{km}^2$ dual-Doppler wind synthesis. All fields are plotted at 0.5 km AGL and all axis labels are in km.

Upon reaching the updraft, vorticity becomes more streamwise and larger in magnitude, likely owing to the generation of streamwise vorticity by the "riverbend" effect and subsequent stretching of this streamwise vorticity (Dahl 2017). As the parcels ascend into the OW minimum, significant vertical vorticity develops (Figs. 15a,b), likely owing to the tilting of horizontal vorticity into the vertical and the stretching of this vertical vorticity. Although substantial streamwise vorticity develops as these parcels enter the OW minimum, it is hypothesized that even more streamwise vorticity would have developed had these parcels initially possessed more streamwise vorticity in the near-storm environment.

Many of the trajectories destined for the northern and western portions of the OW minimum in Fig. 14b are similar to the two in Fig. 15. There is, however, a second group of trajectories that contribute to the central, southern, and eastern portions of the OW minimum (pink trajectories near (2.0, −2.5) in Fig. 14b) that descend from aloft with little horizontal motion owing to the weak horizontal winds in this region (e.g., near the 2-km-radius circulation maximum in Fig. 5c). These trajectories quickly exit the data domain when integrated backward in time and, therefore, could not be examined in detail.

Plots of 0.2–0.8 km AGL SRH confirm that the parcels contributing to the OW minimum originate from a near-storm inflow that possesses little SRH and weak horizontal vorticity (Fig. 16). As mentioned earlier, previous studies (e.g., Davies-Jones 1984; Coffer and Parker 2017) have demonstrated that ingesting parcels with crosswise environmental vorticity and little SRH results in a supercell with a more disorganized low-level updraft and a weaker low-level mesocyclone owing

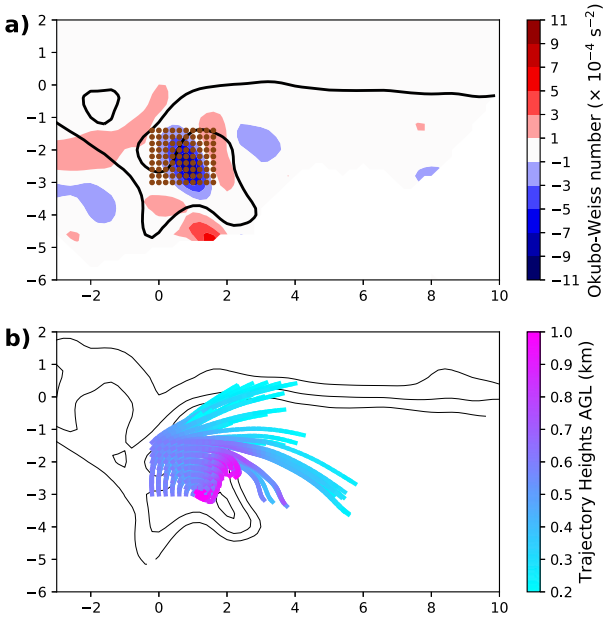

FIG. 14. (a) The initial position of all ninety 15-min backward parcel trajectories at 2236:51 UTC (brown dots) overlaid on 0.6 km AGL Okubo–Weiss number (color shading) and the 0.4 km AGL 15-dBZ reflectivity contour (black line). (b) Horizontal projections of all ninety 15-min backward trajectories, colored by height AGL, overlaid on the 0.4 km AGL dual-Doppler reflectivity at 2236:51 UTC (black contours, every 10 dBZ contoured). Parcel trajectories are truncated where they fall below the 0.2-km AGL data horizon. All axis labels are in km.

to a displacement between the updraft and vertical vorticity maxima. Thus, the weakness of the low-level mesocyclone and the disorganization of the low-level vertical velocity field in the Prospect Valley storm is likely due in part to the low-level updraft ingesting environmental parcels with predominantly crosswise vorticity and little SRH.

c. *Fate of parcels in the forward flank: Forward trajectory analysis*

A region with large magnitudes of horizontal vorticity and large 0.2–0.8 km AGL SRH values exists in the forward flank, which is indicative of large amounts of streamwise vorticity (Fig. 16). Do any parcels originating in this region contribute to the OW minimum, updraft pulse, or low-level mesocyclone? To determine the fate of parcels within this region of enhanced SRH values, trajectories are computed using parcels initiated in a north-south line at various heights within the region of enhanced SRH at 2227:00 UTC and integrated forward in time until 2237:00 UTC with a time step of 10 s. Unlike the backward trajectories in the previous section, none of the forward parcel trajectories spend >25% of their time below the data horizon and only 2 of the 30 parcel trajectories spend >10% of their time below the data horizon. Owing to the brevity of time spent by the parcels in this trajectory set below the data horizon, none of the parcel trajectories are truncated below the data horizon in Fig. 17.

The horizontal projections of these forward trajectories are presented in Fig. 17. The trajectories initiated closer to the surface curve southward and pass through the neck of the hook, but do not become entrained into the updraft pulse. Trajectories initiated farther aloft curve less than the trajectories closer to the surface and instead pass out the rear of the storm. Neither group of trajectories makes it to the updraft region or contributes to the near-surface circulation, OW minimum, or low-level mesocyclone. Interestingly, the SRH field presented in Fig. 16 and the trajectories in Fig. 17 are reminiscent of the streamwise vorticity current (SVC), which has become a focal point of recent high-resolution numerical modeling experiments (e.g., Orf et al. 2017). The trajectories in Fig. 17 follow a similar path to the trajectories within an SVC simulated by Orf et al. (2017) (their Fig. 14), but instead of passing through the RFD and entering the low-level mesocyclone from the southwest, the trajectories in the Prospect Valley storm pass the low-level mesocyclone to the north and west and then appear to start to exit the storm. The parcel trajectories in the Prospect Valley storm are also similar to those observed in the tornadic Goshen County storm, but the trajectories in that storm also passed through the RFD and entered the low-level mesocyclone from the southwest (Kosiba et al. 2013, their Figs. 13 and 14), similar to the trajectories in Orf et al. (2017). It is tempting to argue that given a longer time period of integration and wind data to fill the hole along the baseline that the trajectories will eventually turn eastward and enter the low-level mesocyclone, but this is unlikely given that the storm-relative winds observed by the mobile mesonet south of the low-level mesocyclone are northerly and point away from the low-level mesocyclone (e.g., Fig. 10a). The inability for the parcels from this region of enhanced SRH values to reach the low-level mesocyclone, along with the low-level updraft ingesting air parcels from a near-storm environmental air mass with low SRH values are two factors that likely prevented the development of a strong low-level mesocyclone needed for vortex intensification in the Prospect Valley storm.

6. The inability of streamwise vorticity-rich parcels to reach the low-level mesocyclone

One of the most intriguing questions related to the Prospect Valley storm is why the parcels that possessed

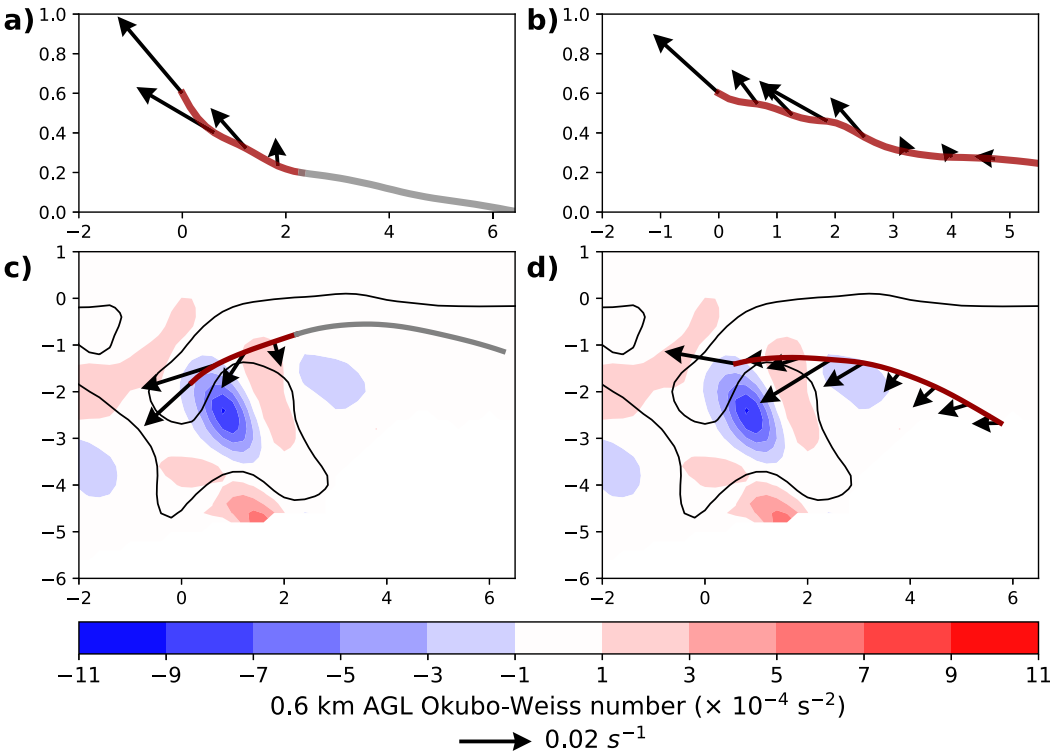

FIG. 15. Two select backward trajectories from the set of ninety 15-min backward trajectories initiated 0.6 km AGL at 2236:51 UTC. (a),(b) The two trajectories in the s–z plane (maroon lines, gray lines show where parcels fall below the 0.2-km AGL data horizon), where s is the streamwise direction; (c),(d) the same trajectories in the x–y plane (maroon lines, gray lines show where parcels fall below the 0.2-km AGL data horizon) overlaid on the 0.6 km AGL Okubo–Weiss number (color shading). Black contours in (c) and (d) represent the 15-dBZ reflectivity contour at 0.4 km AGL. Vorticity vectors are overlaid in all four plots. All axis labels are in km.

large amounts of streamwise vorticity in the forward flank failed to enter the OW minimum or low-level mesocyclone (Fig. 17). As discussed in section 5c, similar parcel trajectories have been seen in both observed and simulated tornadic storms, but in those cases the parcel trajectories terminated at the low-level mesocyclone. Why do the trajectories in the Prospect Valley storm not follow this behavior? To help answer this question, p' retrievals were performed at 2236:51 and 2240:50 UTC (Fig. 18). The p' retrieval has $p' > 0$ northwest of the mesocyclone, which likely coincides with the main downdraft, and $p' < 0$ near the hook echo at the location of the OW minimum (Fig. 18). This behavior matches p' retrievals performed in other observed supercells (e.g., Markowski et al. 2012b, 2018). One noticeable difference between our p' retrievals (Fig. 18) and those performed in the aforementioned cases is that there are very few (if any) HPGA vectors in the quadrant southwest of the low-level mesocyclone (denoted by the magenta crosses in Fig. 18) that point toward the low-level mesocyclone. This is largely owing to the fact that the low-level mesocyclone is not collocated with a p' minima (Fig. 18). Furthermore, there are few HPGA vectors that point toward the OW minimum (which is collocated with a p' minimum) from the south and southwest outside of a radius of ~1 km, which is in contrast with the retrieved pressure fields in Fig. 2d from Markowski et al. (2012b) and Fig. 12b from Markowski et al. (2018). The lack of large regions with pressure gradient accelerations toward the low-level mesocyclone and OW minimum from the south and southwest, coupled with the initial strong, easterly momentum of parcels rich in streamwise vorticity from the forward-flank precipitation (e.g., Fig. 5), likely prevented these parcels from reaching the low-level mesocyclone.

Two features in the retrieved p' field appear to be responsible for creating a pressure gradient field that resulted in the lack of HPGA vectors that point toward the low-level mesocyclone or OW minimum from the south or southwest. The first is a region of weakly negative p' values near $(-1, -3.5)$ in Fig. 18a and $(-2, -5)$ in Fig. 18b that contributes to a pressure gradient that accelerates parcels southward near the spine of the hook echo. The second feature is a p' minimum south of the

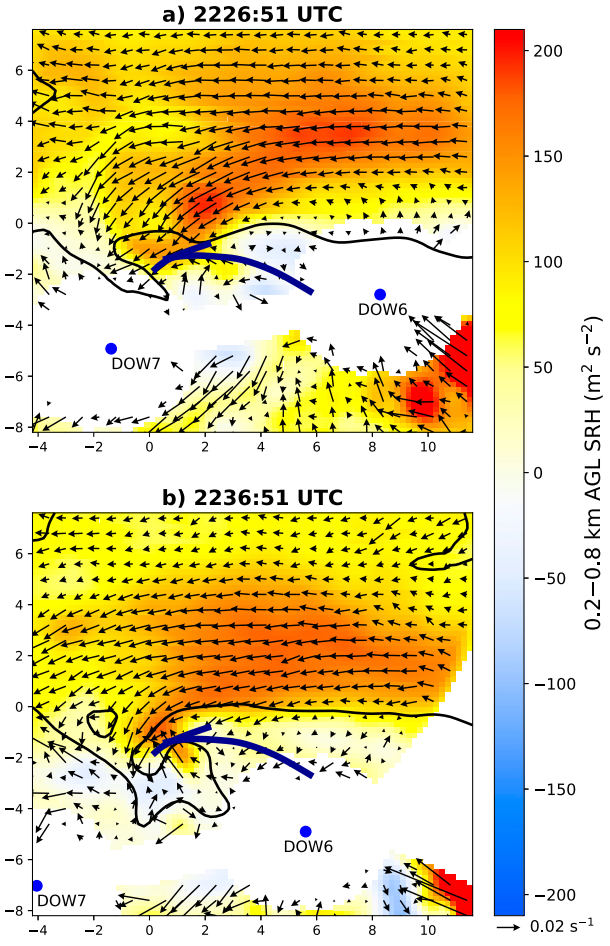

FIG. 16. The 0.2–0.8 km AGL SRH (color shading) and 0.6 km AGL horizontal vorticity vectors (every third vector plotted) at (a) 2226:51 and (b) 2236:51 UTC using the dual-Doppler wind syntheses and Eq. (4) from Davies-Jones et al. (1990). Blue dots denote the locations of the DOWs, the black contour is the 15-dBZ reflectivity contour at 0.4 km AGL, and the dark blue lines are the two parcel trajectories from Fig. 15 (truncated where they fall below the 0.2-km AGL data horizon). Axis labels are in km.

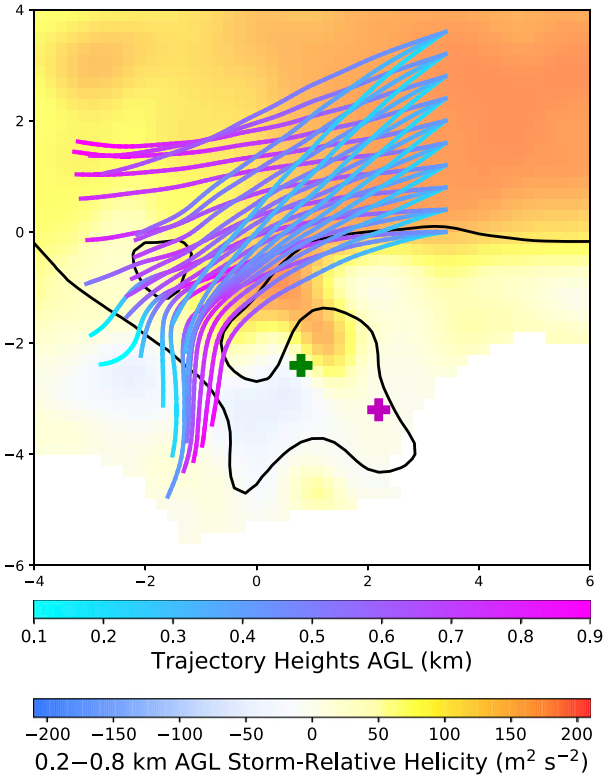

FIG. 17. Horizontal projection of all 30 10-min forward trajectories initiated along the line $x = 3.4$ km at 2227:00 UTC, colored by height AGL. Background color shading represents the 0.2–0.8 km AGL SRH, the black contour is the 15-dBZ dual-Doppler reflectivity outline at 2236:51 UTC, and the green and magenta crosses represent the Okubo–Weiss number minimum and 2-km-radius circulation maximum, respectively. Axis labels are in km.

hook echo near (1, −5) in Fig. 18a, which is collocated with the warm downdraft (Fig. 10a). This second feature likely does not impact the trajectories of the streamwise vorticity-rich parcels in Fig. 17, but this p' minimum still results in HPGA vectors that point away from the low-level mesocyclone center and therefore oppose convergence toward the low-level mesocyclone. The fact that the warm downdraft is collocated with a pressure minimum is surprising because mesoscale downdrafts are often associated with regions of $p' > 0$ owing to the "splat" term in the diagnostic pressure equation (e.g., section 2.5.3, Markowski and Richardson 2010) and owing to the fact that downdrafts often coincide with buoyancy minima, which contributes to $p' > 0$ owing to hydrostatic effects (e.g., section 2.5.2, Markowski and Richardson 2010). In this case, however, the fact that the downdraft is more buoyant that its surroundings may contribute to $p' < 0$, resulting in the observed p' minimum. It is also possible that the observed p' minimum at (1, −5) in Fig. 18a is an artifact, owing to its proximity to the edge of the retrieval domain.

It is also important to note that it is unknown whether the warm downdraft had a net positive or net negative impact on vortex intensification in the Prospect Valley storm. Although the warm downdraft may have contributed to a p' field that opposes radial convergence toward the low-level mesocyclone, the warm downdraft is also a source of air parcels with little negative buoyancy that might increase the chances of vortex intensification if these parcels enter SCV 5. The warm downdraft may have also had other impacts on vortex intensification, such as altering the vertical velocity field and therefore impacting the evolution of the 3D vorticity field (e.g., negative stretching of vertical vorticity beneath the downdraft).

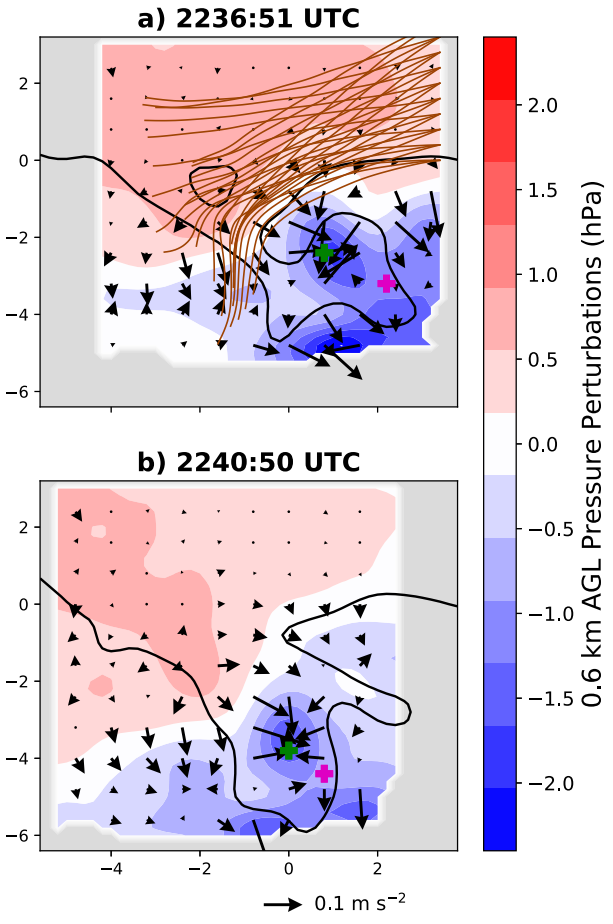

FIG. 18. Retrieved pressure perturbations (color shading, with gray shading indicating regions of missing data) and horizontal pressure gradient acceleration vectors at 0.6 km AGL for (a) 2236:51 UTC and (b) 2240:50 UTC. Pressure perturbations are smoothed using a two-step Leise (1982) filter. The black contour represents the 15-dBZ reflectivity contour at 0.4 km AGL. The brown lines in (a) are the horizontal projections of the 30 forward parcel trajectories shown in Fig. 17. The green and magenta crosses represent the Okubo–Weiss number minimum and 2-km-radius circulation maximum, respectively. Axis labels are in km.

In addition to the roles of the two p' minima discussed above, an alternative hypothesis is that the streamwise vorticity-rich parcels were unable to reach the low-level mesocyclone owing to the weak character of the low-level mesocyclone and the disorganization of the low-level updraft in the Prospect Valley storm. If the cyclonic wind field associated with the low-level mesocyclone had been stronger, an associated strong, dynamic p' minimum would have developed close to the low-level mesocyclone center. This p' minimum would accelerate parcels toward the low-level mesocyclone center and allow the Prospect Valley storm to "capture" parcels rich in streamwise vorticity from the forward flank. By "capturing" these parcels, the low-level mesocyclone could further intensify, resulting in a strong upward-directed VPPGF that could have stretched the vertical vorticity associated with SCV 5, leading to vortex intensification. A more organized low-level updraft may have also been able to "capture" these parcels rich in streamwise vorticity owing to increased convergence near the low-level mesocyclone. The low-level mesocyclone may have initially been too weak and the low-level updraft too disorganized to "capture" these parcels from the forward flank owing to a lack of sufficient environmental streamwise vorticity (as indicated by the relatively small values of 0–500 m and 0–1 km SRH, see Table 2) and the presence of significant environmental crosswise vorticity (Fig. 1).

It is also possible that another process absent from the Prospect Valley storm, but present in tornadic storms that form in similar environments, could have accelerated the streamwise vorticity-rich parcels from the forward flank into the low-level mesocyclone. One such process could be an RFO momentum surge. Several studies have documented the importance of RFO momentum surges in instigating tornadogenesis within supercells owing to the increased convergence and vorticity tilting near the low-level mesocyclone (e.g., Lee et al. 2012; Kosiba et al. 2013; Schenkman et al. 2016). If such a surge was present in the Prospect Valley storm west of the low-level mesocyclone, it is possible that the streamwise vorticity-rich parcels from the forward-flank precipitation may have experienced an acceleration toward the low-level mesocyclone, causing the parcels to enter and intensify the low-level mesocyclone. With a more intense low-level mesocyclone, vortex intensification may have occurred owing to increased stretching of near-surface vertical vorticity. Unfortunately, because this is an observational study, we have no way of knowing how the Prospect Valley storm would have evolved had an RFO surge been present during the analysis period.

7. Summary

The aim of this article was to document factors that prevented the development of a significant tornado in the 26 May 2010 supercell intercepted by VORTEX2 near Prospect Valley, Colorado. The 2225–2245 UTC time period was studied in detail owing to the availability of dual-Doppler DOW data and the presence of an SCV that met the commonly used radar definition of a tornado (40 m s^{-1} inbound-outbound velocity difference). Tornadogenesis is a delicate and intricate process, and explaining exactly why tornadogenesis did not occur (or why a near-surface vortex did not intensify) on a given day, in a given supercell, at a given time

is impossible from an observational perspective because there is no way of knowing how a storm would have evolved had certain conditions not existed. That being said, the following three aspects of the Prospect Valley storm likely prevented the development of a significant tornado during the observation time period despite the presence of far-field circulation comparable to that of two tornadic storms and indications of a low-level upward-directed dynamic VPPGF larger than that of the tornadic Goshen County storm:

1) High environmental LCLs likely contributed to substantial negative buoyancy in some parts of the outflow, as seen in the large, negative values of θ_v' observed by the mobile mesonet near the spine of the hook echo. This substantial negative buoyancy likely made it more difficult for near-surface parcels to be contracted and lifted by the low-level mesocyclone, which contributed to the inability for the far-field circulation to be converged.
2) Air parcels with little streamwise vorticity in the lowest 1 km of the near-storm inflow were ingested by the storm, which likely contributed to an unsteady vertical velocity field that was unable to stretch the vertical vorticity associated with SCV 5. This vertical velocity field featured an updraft pulse coupled with a strong upward-directed dynamic VPPGF proxy that was displaced from the low-level mesocyclone center. This displacement contributed to the inability for the low-level mesocyclone to converge far-field circulation and caused the updraft pulse to be advected rearward in the storm, which contributed to the demise of the updraft pulse.
3) Parcels with abundant streamwise vorticity from the forward flank approached the low-level mesocyclone, but did not reach the OW minimum, updraft pulse, or low-level mesocyclone. The inability of these parcels to reach any of these three features may be partially attributed to two p' minima south and west of the low-level mesocyclone that contributed to HPGA vectors that pointed away away from the low-level mesocyclone. These parcels also did not benefit from a strong low-level mesocyclone or an RFO momentum surge to help them become "captured" by the low-level mesocyclone as has been observed in other tornadic cases.

The weaker low-level mesocyclone and downdrafts observed above SCV 5 during this period prevented the stretching of the near-surface vertical vorticity associated with SCV 5 into a significant tornado. The cumulative effect of the three processes listed above is summarized in Fig. 19.

The results from this study suggest that vortex intensification and tornadogenesis may depend more heavily

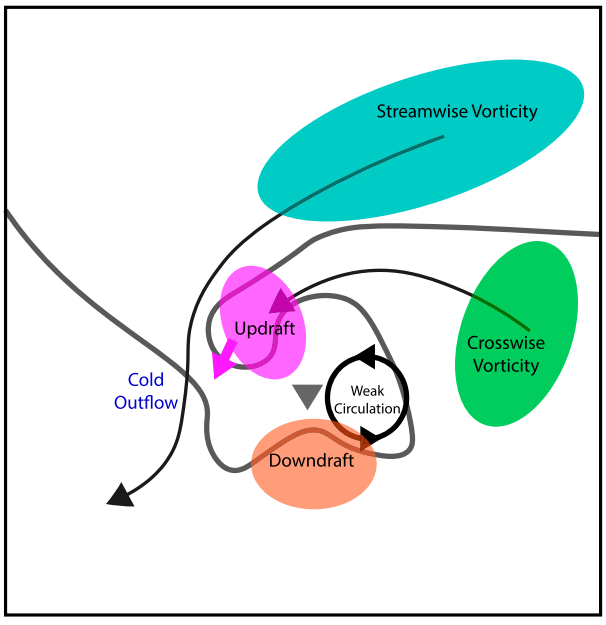

FIG. 19. Schematic detailing the various processes that prevented SCV 5 from intensifying in the Prospect Valley storm. Black arrows denote parcel trajectories, bolded magenta arrow denotes the direction the updraft is being advected by the low-level mesocyclone (denoted here as the "weak circulation"), downward gray triangle denotes the location of the near-surface vortex (SCV 5), and the gray contour denotes the reflectivity outline of the hook echo.

on internal processes if the environment in which the supercell forms is only marginally favorable for tornadoes. For example, had there been more streamwise vorticity in the near-storm environment, the low-level mesocyclone of the Prospect Valley storm would have likely been stronger and may have been able to "capture" parcels rich in streamwise vorticity from the forward flank, causing the low-level mesocyclone to further intensify and provide the dynamic lifting needed for the intensification of SCV 5 into a significant tornado. Furthermore, lower environmental LCLs may have resulted in outflow with less negative buoyancy, requiring less dynamic lifting to stretch near-surface vertical vorticity. Because this was not the case, some process internal to the supercell, such as an RFO momentum surge, would have been needed to accelerate parcels rich in streamwise vorticity from the forward flank into the low-level mesocyclone and cause it to intensify. Without a strong low-level mesocyclone, the Prospect Valley storm was unable to lift the vertical vorticity-rich parcels in the outflow. Thus, future research should focus on internal processes that may promote tornadogenesis in marginal environments and focus on the predictability of such processes.

Finally, researchers should continue to examine observational datasets of supercells collected during

VORTEX2 and other field projects to evaluate output from high-resolution numerical simulations (e.g., Orf et al. 2017) and to create a database of observational cases that can be used for latitudinal studies, similar to Markowski et al. (2002) and French et al. (2015). Such studies can be used to draw more definitive conclusions about the differences between tornadic and nontornadic supercells.

Acknowledgments. This work greatly benefited from discussions with Matt Kumjian at Penn State, who served on the M.S. thesis committee for the first author, as well as Branden Katona, Alicia Klees, and Dylan Steinkruger at Penn State. David Dowell is also thanked for writing the software used to grid the radar data and perform the dual-Doppler wind syntheses. Finally, we thank Jim Marquis and two anonymous reviewers for providing constructive feedback that greatly improved the quality and clarity of this article. Figures 1, 9, and 10 were created using the MetPy package in Python (May et al. 2018) and Figures 2 and 3 were created using the Py-ART package in Python (Helmus and Collis 2016). This project would not have been possible without the tireless work of all participants in the VORTEX2 field project, who collected the data analyzed here. This project was supported by National Science Foundation Award AGS-1536460. Data and software used for this project are available through the Penn State data commons (datacommons.psu.edu).

REFERENCES

Alexander, C., and J. Wurman, 2008: Updated mobile radar climatology of supercell tornado structures and dynamics. *24th Conf. on Severe Local Storms*, Savannah, GA, Amer. Meteor. Soc., 19.4, https://ams.confex.com/ams/pdfpapers/141821.pdf.

Anderson-Frey, A. K., Y. P. Richardson, A. R. Dean, R. L. Thompson, and B. T. Smith, 2016: Investigation of near-storm environment for tornado events and warnings. *Wea. Forecasting*, **31**, 1771–1790, https://doi.org/10.1175/WAF-D-16-0046.1.

Barnes, S. L., 1964: A technique for maximizing details in numerical weather map analysis. *J. Appl. Meteor.*, **3**, 396–409, https://doi.org/10.1175/1520-0450(1964)003<0396:ATFMDI>2.0.CO;2.

Beck, J., and C. Weiss, 2013: An assessment of low-level baroclinity and vorticity within a simulated supercell. *Mon. Wea. Rev.*, **141**, 649–669, https://doi.org/10.1175/MWR-D-11-00115.1.

——, J. L. Schroeder, and J. M. Wurman, 2006: High-resolution dual-Doppler analyses of the 29 May 2001 Kress, Texas, cyclic supercell. *Mon. Wea. Rev.*, **134**, 3125–3148, https://doi.org/10.1175/MWR3246.1.

Bowlan, M. A., 2013: Intensification of low-level mesocyclones and associated stormscale evolution in supercell thunderstorms. M.S. thesis, School of Meteorology, University of Oklahoma, 104 pp.

Brandes, E. A., 1977: Flow in severe thunderstorms observed by dual-Doppler radar. *Mon. Wea. Rev.*, **105**, 113–120, https://doi.org/10.1175/1520-0493(1977)105<0113:FISTOB>2.0.CO;2.

——, 1978: Mesocyclone evolution and tornadogenesis: Some observations. *Mon. Wea. Rev.*, **106**, 995–1011, https://doi.org/10.1175/1520-0493(1978)106<0995:MEATSO>2.0.CO;2.

Browning, K. A., 1964: Airflow and precipitation trajectories within severe local storms which travel to the right of the winds. *J. Atmos. Sci.*, **21**, 634–639, https://doi.org/10.1175/1520-0469(1964)021<0634:AAPTWS>2.0.CO;2.

Coffer, B. E., and M. D. Parker, 2017: Simulated supercells in nontornadic and tornadic VORTEX2 environments. *Mon. Wea. Rev.*, **145**, 149–180, https://doi.org/10.1175/MWR-D-16-0226.1.

——, and ——, 2018: Is there a ''tipping point'' between simulated nontornadic and tornadic supercells in VORTEX2 environments? *Mon. Wea. Rev.*, **146**, 2667–2693, https://doi.org/10.1175/MWR-D-18-0050.1.

——, ——, J. M. L. Dahl, L. J. Wicker, and A. J. Clark, 2017: Volatility of tornadogenesis: An ensemble of simulated nontornadic and tornadic supercells in VORTEX2 environments. *Mon. Wea. Rev.*, **145**, 4605–4625, https://doi.org/10.1175/MWR-D-17-0152.1.

——, ——, R. L. Thompson, B. T. Smith, and R. E. Jewell, 2019: Using near-ground storm relative helicity in supercell tornado forecasting. *Wea. Forecasting*, **34**, 1417–1435, https://doi.org/10.1175/WAF-D-19-0115.1.

Craven, J. P., and H. E. Brooks, 2004: Baseline climatology of sounding derived parameters associated with deep moist convection. *Natl. Wea. Dig.*, **28**, 13–24.

Dahl, J. M. L., 2015: Near-ground rotation in simulated supercells: On the robustness of the baroclinic mechanism. *Mon. Wea. Rev.*, **143**, 4929–4942, https://doi.org/10.1175/MWR-D-15-0115.1.

——, 2017: Tilting of horizontal shear vorticity and the development of updraft rotation in supercell thunderstorms. *J. Atmos. Sci.*, **74**, 2997–3020, https://doi.org/10.1175/JAS-D-17-0091.1.

Davies-Jones, R., 1984: Streamwise vorticity: The origin of updraft rotation in supercell storms. *J. Atmos. Sci.*, **41**, 2991–3006, https://doi.org/10.1175/1520-0469(1984)041<2991:SVTOOU>2.0.CO;2.

——, 2015: A review of supercell and tornado dynamics. *Atmos. Res.*, **158–159**, 274–291, https://doi.org/10.1016/j.atmosres.2014.04.007.

——, and H. Brooks, 1993: Mesocyclogenesis from a theoretical perspective. *The Tornado: Its Structure, Dynamics, Prediction, and Hazards*, *Geophys. Monogr.*, Vol. 79, Amer. Geophys. Union, 105–114.

——, D. Burgess, and M. Foster, 1990: Test of helicity as a tornado forecast parameter. Preprints, *16th Conf. on Severe Local Storms*, Alberta, Canada, Amer. Meteor. Soc., 588–592.

Doswell, C. A., and P. M. Markowski, 2004: Is buoyancy a relative quantity? *Mon. Wea. Rev.*, **132**, 853–863, https://doi.org/10.1175/1520-0493(2004)132<0853:IBARQ>2.0.CO;2.

Dowell, D. C., and A. Shapiro, 2003: Stability of an iterative dual-Doppler wind synthesis in Cartesian coordinates. *J. Atmos. Oceanic Technol.*, **20**, 1552–1559, https://doi.org/10.1175/1520-0426(2003)020<1552:SOAIDW>2.0.CO;2.

French, M. M., D. W. Burgess, E. R. Mansell, and L. J. Wicker, 2015: Bulk hook echo raindrop sizes retrieved using mobile, polarimetric Doppler radar observations. *J. Appl. Meteor. Climatol.*, **54**, 423–450, https://doi.org/10.1175/JAMC-D-14-0171.1.

Gal-Chen, T., 1978: A method for the initialization of the anelastic equations: Implications for matching models with observations. *Mon. Wea. Rev.*, **106**, 587–606, https://doi.org/10.1175/1520-0493(1978)106<0587:AMFTIO>2.0.CO;2.

Grzych, M. L., B. D. Lee, and C. A. Finley, 2007: Thermodynamic analysis of supercell rear-flank downdrafts from project

ANSWERS. *Mon. Wea. Rev.*, **135**, 240–246, https://doi.org/10.1175/MWR3288.1.

Guarriello, F., C. J. Nowotarski, and C. C. Epifanio, 2018: Effects of the low-level wind profile on outflow position and near-surface vertical vorticity in simulated supercell thunderstorms. *J. Atmos. Sci.*, **75**, 731–753, https://doi.org/10.1175/JAS-D-17-0174.1.

Hane, C. E., and P. S. Ray, 1985: Pressure and buoyancy fields derived from Doppler radar data in a tornadic thunderstorm. *J. Atmos. Sci.*, **42**, 18–35, https://doi.org/10.1175/1520-0469(1985)042<0018:PABFDF>2.0.CO;2.

Helmus, J. J., and S. M. Collis, 2016: The Python ARM Radar Toolkit (Py-ART), a library for working with weather radar data in the Python programming language. *J. Open Res. Software*, **4**, e25, https://doi.org/10.5334/jors.119.

Klees, A. M., Y. P. Richardson, P. M. Markowski, C. Weiss, J. M. Wurman, and K. K. Kosiba, 2016: Comparison of the tornadic and nontornadic supercells intercepted by VORTEX2 on 10 June 2010. *Mon. Wea. Rev.*, **144**, 3201–3231, https://doi.org/10.1175/MWR-D-15-0345.1.

Klemp, J. B., and R. Rotunno, 1983: A study of the tornadic region within a supercell thunderstorm. *J. Atmos. Sci.*, **40**, 359–377, https://doi.org/10.1175/1520-0469(1983)040<0359:ASOTTR>2.0.CO;2.

Koch, S. E., M. desJardins, and P. J. Kocin, 1983: An interactive Barnes objective map analysis scheme for use with satellite and conventional data. *J. Climate Appl. Meteor.*, **22**, 1487–1503, https://doi.org/10.1175/1520-0450(1983)022<1487:AIBOMA>2.0.CO;2.

Kosiba, K., J. Wurman, Y. Richardson, P. Markowski, P. Robinson, and J. Marquis, 2013: Genesis of the Goshen County, Wyoming, tornado on 5 June 2009 during VORTEX2. *Mon. Wea. Rev.*, **141**, 1157–1181, https://doi.org/10.1175/MWR-D-12-00056.1.

Lee, B. D., C. A. Finley, and C. D. Karstens, 2012: The Bowdle, South Dakota, cyclic tornadic supercell of 22 May 2010: Surface analysis of rear-flank downdraft evolution and multiple internal surges. *Mon. Wea. Rev.*, **140**, 3419–3441, https://doi.org/10.1175/MWR-D-11-00351.1.

Leise, J. A., 1982: A multidimensional scale-telescoped filter and data extension package. NOAA Tech. Memo. ERL WPL-82, NOAA Office of Oceanic and Atmospheric Research, Silver Spring, Maryland, 19 pp.

Lemon, L. R., and C. A. Doswell, 1979: Severe thunderstorm evolution and mesocyclone structure as related to tornadogenesis. *Mon. Wea. Rev.*, **107**, 1184–1197, https://doi.org/10.1175/1520-0493(1979)107<1184:STEAMS>2.0.CO;2.

Majcen, M., P. Markowski, Y. Richardson, D. Dowell, and J. Wurman, 2008: Multipass objective analyses of Doppler radar data. *J. Atmos. Oceanic Technol.*, **25**, 1845–1858, https://doi.org/10.1175/2008JTECHA1089.1.

Markowski, P., and Y. Richardson, 2009: Tornadogenesis: Our current understanding, forecasting considerations, and questions to guide future research. *Atmos. Res.*, **93**, 3–10, https://doi.org/10.1016/j.atmosres.2008.09.015.

——, and ——, 2010: *Mesoscale Meteorology in Midlatitudes.* Wiley-Blackwell, 430 pp.

——, and ——, 2014: The influence of environmental low-level shear and cold pools on tornadogenesis: Insights from idealized simulations. *J. Atmos. Sci.*, **71**, 243–275, https://doi.org/10.1175/JAS-D-13-0159.1.

——, ——, E. Rasmussen, J. Straka, R. Davies-Jones, and R. J. Trapp, 2008: Vortex lines within low-level mesocyclones obtained from pseudo-dual-Doppler radar observations. *Mon. Wea. Rev.*, **136**, 3513–3535, https://doi.org/10.1175/2008MWR2315.1.

——, M. Majcen, Y. Richardson, J. Marquis, and J. Wurman, 2011: Characteristics of the wind field in three nontornadic low-level mesocyclones observed by the Doppler on Wheels radars. *Electron. J. Severe Storms Meteor.*, **6** (3), http://www.ejssm.org/ojs/index.php/ejssm/issue/view/28.

——, and Coauthors, 2012a: The pretornadic phase of the Goshen County, Wyoming, supercell of 5 June 2009 intercepted by VORTEX2. Part I: Evolution of kinematic and surface thermodynamic fields. *Mon. Wea. Rev.*, **140**, 2887–2915, https://doi.org/10.1175/MWR-D-11-00336.1.

——, and Coauthors, 2012b: The pretornadic phase of the Goshen County, Wyoming, supercell of 5 June 2009 intercepted by VORTEX2. Part II: Intensification of low-level rotation. *Mon. Wea. Rev.*, **140**, 2916–2938, https://doi.org/10.1175/MWR-D-11-00337.1.

——, J. M. Straka, and E. N. Rasmussen, 2002: Direct surface thermodynamic observations within the rear-flank downdrafts of nontornadic and tornadic supercells. *Mon. Wea. Rev.*, **130**, 1692–1721, https://doi.org/10.1175/1520-0493(2002)130<1692:DSTOWT>2.0.CO;2.

——, T. P. Hatlee, and Y. P. Richardson, 2018: Tornadogenesis in the 12 May 2010 supercell thunderstorm intercepted by VORTEX2 near Clinton, Oklahoma. *Mon. Wea. Rev.*, **146**, 3623–3650, https://doi.org/10.1175/MWR-D-18-0196.1.

——, N. T. Lis, D. D. Turner, T. R. Lee, and M. S. Buban, 2019: Observations of near-surface vertical wind profiles and vertical momentum fluxes from vortex-se 2017: Comparisons to Monin–Obukhov similarity theory. *Mon. Wea. Rev.*, **147**, 3811–3824, https://doi.org/10.1175/MWR-D-19-0091.1.

May, R., S. Arms, P. Marsh, E. Bruning, and J. Leeman, 2018: MetPy: A Python package for meteorological data. Unidata, accessed 1 October 2019, https://doi.org/10.5065/D6WW7G29.

Okubo, K., 1970: Horizontal dispersion of floatable particles in the vicinity of velocity singularities such as convergences. *Deep-Sea Res.*, **17**, 445–454, https://doi.org/10.1016/0011-7471(70)90059-8.

Orf, L., R. Wilhelmson, B. Lee, C. Finley, and A. Houston, 2017: Evolution of a long-track violent tornado within a simulated supercell. *Bull. Amer. Meteor. Soc.*, **98**, 45–68, https://doi.org/10.1175/BAMS-D-15-00073.1.

Oye, R., C. Mueller, and S. Smith, 1995: Software for radar translation, visualization, editing, and interpolation. Preprints, *27th Conf. on Radar Meteorology*, Vail, CO, Amer. Meteor. Soc., 359–361.

Parker, M. D., 2014: Composite VORTEX2 supercell environments from near-storm soundings. *Mon. Wea. Rev.*, **142**, 508–529, https://doi.org/10.1175/MWR-D-13-00167.1.

Pauley, P. M., and X. Wu, 1990: The theoretical, discrete, and actual response of the Barnes objective analysis scheme for one- and two-dimensional fields. *Mon. Wea. Rev.*, **118**, 1145–1164, https://doi.org/10.1175/1520-0493(1990)118<1145:TTDAAR>2.0.CO;2.

Rasmussen, E. N., and D. O. Blanchard, 1998: A baseline climatology of sounding-derived supercell and tornado forecast parameters. *Wea. Forecasting*, **13**, 1148–1164, https://doi.org/10.1175/1520-0434(1998)013<1148:ABCOSD>2.0.CO;2.

——, J. M. Straka, R. Davies-Jones, C. A. Doswell, F. H. Carr, M. D. Eilts, and D. R. MacGorman, 1994: Verification of the origins of rotation in tornadoes experiment: VORTEX. *Bull. Amer. Meteor. Soc.*, **75**, 995–1006, https://doi.org/10.1175/1520-0477(1994)075<0995:VOTOOR>2.0.CO;2.

Rotunno, R., 1981: On the evolution of thunderstorm rotation. *Mon. Wea. Rev.*, **109**, 577–586, https://doi.org/10.1175/1520-0493(1981)109<0577:OTEOTR>2.0.CO;2.

——, and J. B. Klemp, 1982: The influence of the shear-induced pressure gradient on thunderstorm motion. *Mon. Wea. Rev.*, **110**, 136–151, https://doi.org/10.1175/1520-0493(1982)110<0136:TIOTSI>2.0.CO;2.

——, and ——, 1985: On the rotation and propagation of simulated supercell thunderstorms. *J. Atmos. Sci.*, **42**, 271–292, https://doi.org/10.1175/1520-0469(1985)042<0271:OTRAPO>2.0.CO;2.

——, P. M. Markowski, and G. H. Bryan, 2017: "Near ground" vertical vorticity in supercell thunderstorm models. *J. Atmos. Sci.*, **74**, 1757–1766, https://doi.org/10.1175/JAS-D-16-0288.1.

Schenkman, A. D., M. Xue, and D. T. Dawson II, 2016: The cause of internal outflow surges in a high-resolution simulation of the 8 May 2003 Oklahoma City tornadic supercell. *J. Atmos. Sci.*, **73**, 353–370, https://doi.org/10.1175/JAS-D-15-0112.1.

Shabbott, C. J., and P. M. Markowski, 2006: Surface in situ observations within the outflow of forward-flank downdrafts of supercell thunderstorms. *Mon. Wea. Rev.*, **134**, 1422–1441, https://doi.org/10.1175/MWR3131.1.

Skinner, P. S., C. C. Weiss, M. M. French, H. B. Bluestein, P. M. Markowski, and Y. P. Richardson, 2014: VORTEX2 observations of a low-level mesocyclone with multiple internal rear-flank downdraft momentum surges in the 18 May 2010 Dumas, Texas, supercell. *Mon. Wea. Rev.*, **142**, 2935–2960, https://doi.org/10.1175/MWR-D-13-00240.1.

SPC, 2010: SPC Storm Reports for 05/26/10. Storm Prediction Center, accessed 2 January 2019, https://www.spc.noaa.gov/climo/reports/100526_rpts.html.

——, 2018: Storm Prediction Center WCM Page. Storm Prediction Center, accessed 17 December 2018, https://www.spc.noaa.gov/wcm/.

Straka, J. M., E. N. Rasmussen, and S. E. Fredrickson, 1996: A mobile mesonet for finescale meteorological observations. *J. Atmos. Oceanic Technol.*, **13**, 921–936, https://doi.org/10.1175/1520-0426(1996)013<0921:AMMFFM>2.0.CO;2.

Tanamachi, R. L., H. B. Bluestein, M. Xue, W.-C. Lee, K. A. Orzel, S. J. Frasier, and R. M. Wakimoto, 2013: Near-surface vortex structure in a tornado and in a sub-tornado-strength convective-storm vortex observed by a mobile, W-band radar during VORTEX2. *Mon. Wea. Rev.*, **141**, 3661–3690, https://doi.org/10.1175/MWR-D-12-00331.1.

Thompson, R. L., R. Edwards, J. A. Hart, K. L. Elmore, and P. Markowski, 2003: Close proximity soundings within supercell environments obtained from the Rapid Update Cycle. *Wea. Forecasting*, **18**, 1243–1261, https://doi.org/10.1175/1520-0434(2003)018<1243:CPSWSE>2.0.CO;2.

Trapp, R. J., 1999: Observations of nontornadic low-level mesocyclones and attendant tornadogenesis failure during VORTEX. *Mon. Wea. Rev.*, **127**, 1693–1705, https://doi.org/10.1175/1520-0493(1999)127<1693:OONLLM>2.0.CO;2.

——, and C. A. Doswell, 2000: Radar data objective analysis. *J. Atmos. Oceanic Technol.*, **17**, 105–120, https://doi.org/10.1175/1520-0426(2000)017<0105:RDOA>2.0.CO;2.

Wakimoto, R. M., and H. Cai, 2000: Analysis of a nontornadic storm during VORTEX 95. *Mon. Wea. Rev.*, **128**, 565–592, https://doi.org/10.1175/1520-0493(2000)128<0565:AOANSD>2.0.CO;2.

Waugh, S., and S. Fredrickson, 2010: An improved aspirated temperature system for mobile meteorological observations, especially in severe weather. *25th Conf. on Severe Local Storms*, Denver, CO, Amer. Meteor. Soc., P5.2, https://ams.confex.com/ams/25SLS/webprogram/Paper176205.html.

Weisman, M. L., and J. B. Klemp, 1982: The dependence of numerically simulated convective storms on vertical wind shear and buoyancy. *Mon. Wea. Rev.*, **110**, 504–520, https://doi.org/10.1175/1520-0493(1982)110<0504:TDONSC>2.0.CO;2.

——, and ——, 1984: The structure and classification of numerically simulated convective storms in directionally varying wind shears. *Mon. Wea. Rev.*, **112**, 2479–2498, https://doi.org/10.1175/1520-0493(1984)112<2479:TSACON>2.0.CO;2.

Weiss, J., 1991: The dynamics of enstrophy transfer in two-dimensional hydrodynamics. *Physica D*, **48**, 273–294, https://doi.org/10.1016/0167-2789(91)90088-Q.

Wurman, J., D. Dowell, Y. Richardson, P. Markowski, E. Rasmussen, D. Burgess, L. Wicker, and H. B. Bluestein, 2012: The second Verification of the Origins of Rotation in Tornadoes Experiment: VORTEX2. *Bull. Amer. Meteor. Soc.*, **93**, 1147–1170, https://doi.org/10.1175/BAMS-D-11-00010.1.